

1 Interpreting Summertime Hourly Variation of NO₂ Columns with Implications for 2 Geostationary Satellite Applications

3 Deepangsu Chatterjee¹, Randall V. Martin¹, Chi Li¹, Dandan Zhang¹, Haihui Zhu¹, Daven K. Henze²,
4 James H. Crawford³, Ronald C. Cohen^{4,5}, Lok N. Lamsal⁶, Alexander M. Cede⁶

5 ¹Department of Energy, Environmental & Chemical Engineering, Washington University in St. Louis, St.
6 Louis, MO, USA

7 ²Department of Mechanical Engineering, University of Colorado, Boulder, CO, USA

8 ³NASA Langley Research Center, Hampton, VA, USA

9 ⁴Department of Chemistry, University of California, Berkeley, Berkeley, CA, USA

10 ⁵Department of Earth and Planetary Science, University of California, Berkeley, Berkeley, CA, USA

11 ⁶NASA Goddard Space Flight Center, Greenbelt, MD 20771, USA

12

13 Correspondence: Deepangsu Chatterjee (deepangsuchatterjee@wustl.edu)

14

15 Abstract

16 Accurate representation of the hourly variation of the NO₂ column-to-surface relationship is needed to
17 interpret geostationary constellation observations of tropospheric NO₂ columns. Prior work has revealed
18 inconsistency in the hourly variation in NO₂ columns and surface concentrations. In this study, we use the
19 high-performance configuration of the GEOS-Chem model (GCHP) to interpret the daytime hourly
20 variation in NO₂ total columns and surface concentrations during summer. We use summer-time Pandora
21 sun photometers and aircraft measurements during the Deriving Information on Surface Conditions from
22 Column and Vertically Resolved Observations Relevant to Air Quality (DISCOVER-AQ) field
23 ~~campaigns~~ campaigns over Maryland, Texas, and Colorado as well as 50 sites (31: contiguous USA, 10:
24 Europe, 9: Asia) from the Pandora Global Network (PGN). We correct the Pandora total NO₂ vertical
25 columns for 1) hourly variation in the column effective temperature driven by the fractional boundary layer
26 contribution of atmospheric layers to the total NO₂ column, and 2) change in local solar time along the line-
27 of-sight of the Pandora instrument. The corrected Pandora observations total NO₂ vertical columns are
28 increased by about $5\text{--}6 \times 10^{14}$ molecules cm⁻² at 9 AM and 6 PM across all Pandora sites. We conduct fine
29 resolution (~12 km) simulations over the contiguous US, Europe, and East Asia using the stretched grid
30 capability of GCHP. We also examine the effect of planetary boundary layer height (PBLH) corrections on
31 the total columns. We first evaluate the GCHP simulated absolute NO₂ concentration with Pandora and
32 aircraft observations. We find that fine resolution simulations at 12 km compared with moderate resolution
33 of ~55 km reduce the Normalized Bias (NB) versus against Pandora total columns (19% to 10%) and versus
34 aircraft measurements (25% to 13%) over Maryland, Texas, and Colorado. Fine resolution 12 km
35 simulations at 12 km compared with moderate resolution at 55 km also reduce the NB versus Pandora total
36 columns over the eastern US (17% to 9%), western US (22% to 14%), Europe (24% to 15%), and Asia
37 (29% to 21%) as compared to the 55 km simulations. We next use the 12 km simulations simulations
38 to examine the hourly variation in the NO₂ columns columns and surface concentrations. We explain the weaker
39 hourly variation in NO₂ columns than at the NO₂ surface concentrations as a function of 1) hourly variation
40 in the column effective temperature, 2) hourly variation in the local solar time along the Pandora line-of-
41 sight, and 3) the integral differences in hourly variation of weakly connected atmospheric layers; with the
42 lowest 500 m exhibiting greater NO₂ concentrations in morning and evening than midday, while the residual
43 column above 500 m dominates the total column with weaker variability.

44

Formatted: Default, Left

45

46 **1 Introduction**

47 Nitrogen oxides ($\text{NO}_x \equiv \text{NO} + \text{NO}_2$) affect air quality and human health directly by
48 contributing to premature mortality (Burnett et al., 2004; Tao et al., 2012) and asthma for children
49 and adults (Anenberg et al., 2018), and indirectly by acting as precursors for tropospheric ozone
50 (O_3) formation (Jacob et al., 1996), and nitrate aerosols (Bauer et al., 2007). Significant spatial
51 gaps in ground-based monitoring of surface NO_2 concentrations and pronounced NO_2
52 heterogeneity inhibit exposure assessment. To fill in the knowledge of NO_2 exposures across a
53 greater fraction of the human population, satellite remote sensing offers the potential for spatially
54 comprehensive measurements. Major advances in satellite remote sensing from sun-synchronous
55 low earth orbit (LEO) havehas achieved global characterization of tropospheric NO_2 columns at
56 specific times of the day (Duncan et al., 2013; Veeffkind et al., 2012) that have been applied to
57 infer ground level NO_2 concentrations (Anenberg et al., 2022; Lamsal et al., 2011; Geddes and
58 Martin, 2017; Cooper et al., 2022). The emerging geostationary constellation (Al-Saadi et al.,
59 2017) including the Geostationary Environmental Monitoring Spectrophotometer (GEMS) over
60 Asia, Tropospheric Emissions: Monitoring Pollution (TEMPO) over North America, and Sentinel-
61 4 over Europe offers the prospect of inferring spatially comprehensive maps of hourly ground-
62 level NO_2 concentrations. TowardsToward this goal, there is a need to develop an accurate
63 representation of the hourly NO_2 column to surface relationship.

64 Understanding the hourly variation of the relationship of NO_2 columns with surface
65 concentrations is of particular interest due to its role in the inference of hourly surface NO_2 from
66 satellite remote sensing. Numerous studies have separately examined the role of processes such as
67 surface emissions, boundary layer mixing, chemistry, deposition, and advection (Yang et al.,
68 2023b; Herman et al., 2009; Ghude et al., 2020; Zhang et al., 2016) upon the hourly variation of

69 NO₂ columns and upon surface NO₂ concentrations in the United States (Day et al., 2009), Spain
70 (Van Stratum et al., 2012), India (David and Nair, 2011), South Korea (Yang et al., ~~2023b~~, 2023a,
71 b) and China (Tong et al., 2017). Differences have been identified in the daytime hourly variation
72 of NO₂ tropospheric columns and surface concentrations during the DISCOVER-AQ and KORUS-
73 AQ (Korea US -Air Quality) campaigns with pronounced variation in surface concentrations that
74 is not evident in the columns (Choi et al., 2020; Crawford et al., 2021). Differences have also been
75 noted in hourly variation of NO₂ measured by aircraft and ground-based Pandora instruments (Li
76 et al., 2021). There is a need to understand the factors that can affect the relationship of hourly
77 NO₂ columns with surface concentrations.

78 Major challenges in the interpretation of satellite NO₂ observations include the short
79 lifetime of NO_x (Laughner and Cohen, 2019), and localized emissions (Crippa et al., 2018) that
80 affect its spatial heterogeneity. Course resolution inputs to satellite retrieval algorithms (e.g.,
81 terrain height, albedo, and a priori NO₂ profiles) can lead to biases (Laughner et al., 2019;
82 Laughner et al., 2018; Russell et al., 2011). Complications with ground-based measurements of
83 the NO₂ columns as part of Pandora include uncertainties at steeper solar zenith angles during
84 morning and evening hours (Herman et al., 2009; Reed et al., 2015) and the changing Pandora
85 field of view (FOV) during morning and late evening (Li et al., 2021). Non-linearities in the
86 relationship between NO₂ concentrations and NO_x sources or sinks can lead to biases in coarse-
87 resolution chemical transport models (CTMs) (Valin et al., 2011) that necessitate ~~chemical~~
88 ~~transport models~~CTMs with a finer resolution (Li et al., 2021, 2023a). Recent advances in the
89 simulation of global atmospheric composition at fine resolution (Eastham et al., 2018; Hu et al.,
90 2018; Martin et al., 2022) offer the opportunity to address the resolution need at the global scales
91 of the geostationary constellation.

92 An important consideration in the inference of surface NO₂ concentrations with columnar
93 satellite observations is the vertical profile of NO₂ concentrations. Aircraft observations from the
94 NASA Deriving Information on Surface Conditions from Column and Vertically Resolved
95 Observations Relevant to Air Quality (DISCOVER-AQ) campaign ~~offer~~offers measurements of
96 the NO₂ vertical profile in the lower troposphere for evaluation of modeled vertical profiles (Flynn
97 et al., 2014; Reed et al., 2015). The Pandora Global Network (PGN) is a global sun photometer
98 network that offers hourly measurements of total NO₂ columns (Verhoelst et al., 2021), useful for
99 interpretation of the daytime variation of NO₂ columns and evaluation of simulated columns. In
100 this study, we ~~use~~interpret the summertime NO₂ measurements from the NASA P-3B aircraft ~~and~~
101 ~~Pandora sun photometers over Maryland, Texas, and Colorado during the DISCOVER-AQ~~
102 ~~campaign to understand the hourly variation of the NO₂ vertical distribution. We sample~~using the
103 high-performance GEOS-Chem (GCHP) simulations along aircraft flight tracks and account for
104 line-of-sight of the Pandora sun photometers ~~to interpret the hourly variation of NO₂ vertical~~
105 ~~distribution over Maryland, Texas, and vertical columns. Colorado during the DISCOVER-AQ~~
106 ~~campaign.~~ We also explore the effect of vertical changes in the hourly variation of temperature on
107 the NO₂ cross-section~~7~~ and the raw Pandora columns. We further investigate the hourly variation
108 of NO₂ columns and surface concentrations from 50 PGN sites across the northern hemisphere.
109 Section 2 describes the datasets and methods used in this study to interpret the variation of NO₂
110 columns, surface concentrations, and vertical distribution over DISCOVER-AQ and PGN sites.
111 Section 3 examines the consistency between the NO₂ vertical columns and surface concentrations
112 across DISCOVER-AQ sites, and PGN sites across the contiguous United States (CONUS-)
113 Europe, and Asia. We explore the effects of model resolution and boundary layer height
114 adjustments on the hourly variation of NO₂ total columns and surface concentrations as a function

115 of hourly variation in mixed layer depth and photochemistry, and measurement characteristics of
116 Pandora sun photometers over PGN sites across the CONUS, Europe, and Asia.

117 **2 Materials and Methods**

118 **2.1 Aircraft measurements of NO₂ vertical profiles**

119 The DISCOVER-AQ campaign offers comprehensive datasets of airborne and surface
120 observations relevant for accessing air quality. One of the main objectives of the campaign was to
121 examine the hourly variation of the relationship between the column and surface concentrations.

122 In this study, we use aircraft, Pandora, and surface measurements over Maryland (July 2011),
123 Texas (September 2013) and Colorado (July-August 2014) to investigate the hourly variation of
124 NO₂ vertical profiles during summer when a long duration of daylight exists for analysis. Figure
125 A1 shows the flight tracks, altitude variation, roadways, and Pandora instrument locations over
126 Maryland, Texas, and Colorado during the DISCOVER-AQ campaign. We focus on the aircraft
127 spirals since they are designed to sample the vertical profile. We use NO₂ concentrations measured
128 by the thermal dissociation laser-induced fluorescence (TD-LIF) technique (Thornton et al., 2000;
129 Day et al., 2002) during the campaign. The laser-induced fluorescence method is highly sensitive
130 for directly measuring NO₂, with a measurement uncertainty of 5 % and a detection limit of 30
131 pptv (Thornton et al., 2000). It also attempts to correct for positive interferences (Nault et al., 2015;
132 Yang et al., 2023b). We use aircraft measurements from a height of about 300 m above ground
133 level (AGL) up to 4 km AGL where high measurement frequency facilitates regional
134 representation.

135 **2.2 Pandonia Global Network NO₂ Total Column Densities**

136 PGN is a global network of ground-based sun photometers that ~~measures~~measure sun and
137 sky

Formatted: Indent: First line: 0"

138 radiance from 270 to 530 nm that allow retrievals of various trace gases including NO₂. Retrieval
139 precision for total vertical NO₂ columns (“NO₂ columns” hereafter) is 5.4×10^{14} molecules/cm²
140 with a nominal accuracy of 2.7×10^{15} molecules/cm² under clear-sky conditions (Herman et al.,
141 2009; Cede 2021). We ~~use~~obtained the level 2 data product from the version rrvs3p1-8 for PGN
142 and ~~for DISCOVER~~DISCOVER-AQ ~~the~~ (data ~~available from~~
143 ~~<https://asdc.larc.nasa.gov/data/DISCOVER-AQ/>~~source listed in the code and data availability
144 section). We also include surface NO₂ observations from co-located DISCOVER-AQ and PGN
145 sites. We use NO₂ columns and surface concentrations employed during the DISCOVER-AQ
146 campaign from 18 sites over Maryland, Texas and Colorado. We also include NO₂ columns and
147 surface concentrations from 50 PGN sites (the US: 31, Europe: 10, Asia: 9) for June-July-August
148 (JJA) 2019. We focus on the NO₂ observations between 9 AM - 6 PM local solar time, for
149 consistency in observation frequency across all PGN sites. Tables A1 and A2 contain the names
150 and ~~location~~locations of the DISCOVER-AQ and PGN sites respectively. We exclude Pandora
151 measurements with SZA>80°. We use total NO₂ columns including the stratosphere because the
152 use of external information sources to remove the stratospheric NO₂ columns from PGN can
153 introduce errors in the residual tropospheric columns (Choi et al., 2020).

Formatted: Underline, Font color: Hyperlink

154 2.3 GEOS-Chem simulations

155 We use GCHP, the high-performance configuration of the GEOS-Chem model that
156 operates with a distributed-memory framework for massive parallelization (Eastham et al., 2018),
157 to interpret the NO₂ column, vertical distribution and surface observations. GCHP offers the ability
158 to simulate the entire atmospheric column needed to interpret Pandora measurements ~~at~~and the
159 fine spatial resolution needed to interpret aircraft measurements. GEOS-Chem is driven by
160 assimilated meteorological data from the NASA Goddard Earth Observation System (GEOS).

161 GEOS-Chem includes a comprehensive O_x-NO_x-VOC-halogen-aerosol chemical mechanism in
162 the troposphere, in addition to the unified tropospheric-stratospheric chemistry extension in the
163 stratosphere (Eastham et al., 2014). We use GEOS-Chem 14.1.1 which includes recent updates to
164 GCHP (Martin et al., 2022), NO_x heterogenous and cloud chemistry (Holmes et al., 2019), isoprene
165 chemistry (Bates and Jacob, 2019), and aromatic chemistry (Bates et al., 2021). The ISORROPIA
166 II module simulates the thermodynamic partitioning between the gas and condensed phase
167 (Fountoukis and Nenes, 2007). Natural emissions include biogenic [volatile organic compounds](#)
168 [\(VOCs\)](#) (Weng et al., 2020), lightning NO_x (Murray et al., 2012), and soil NO_x (Weng et al., 2020).
169 GEOS-Chem includes an updated aircraft NO_x emissions inventory for 2019, developed with the
170 Aircraft Emissions Inventory Code (Simone et al., 2013). Figure A2 shows the hourly variation of
171 NO_x emissions across the PGN sites. For [the](#) interpretation of PGN measurements in 2019, we
172 conduct the simulations for the year 2019 using GEOS-FP meteorology and the stretched grid
173 capability (Bindle et al., 2021) at a cubed sphere resolution of C180 (~55 km) and stretch factor
174 of 4.0 yielding a regional refinement of ~12 km. All simulations were conducted with a two-week
175 spin-up. We interpolate hourly GCHP outputs of simulated NO₂ columns and surface
176 concentrations to the local solar time at the PGN observation sites.

177 For interpretation of the DISCOVER-AQ aircraft campaigns, we conduct stretched grid
178 simulations over Maryland (July 2011), Texas (September 2013) and Colorado (July-August 2014)
179 with identical stretched grid configurations, with sampling along the aircraft flight tracks. We use
180 MERRA-2 meteorology for these simulations as GEOS-FP meteorology datasets are not available
181 prior to 2014. A sensitivity test for the year 2019 using either GEOS-FP and MERRA-2 affects
182 the local simulated NO₂ columns and surface concentrations by less than 5% for both 12 km and
183 55 km resolutions.

184 Hourly variation of the planetary boundary layer height (PBLH) can influence the vertical
 185 distribution and hence the surface concentration of aerosols and trace gases (Lin and McElroy,
 186 2010). Millet et al., (2015) found that GEOS-FP reanalysis over-estimates daytime PBLH as
 187 compared to observations; correcting for PBLH estimations can lead to a better agreement of ozone
 188 (Oak et al., 2019) and PM_{2.5} (Li et al., 2023b) with measurements. Our base case simulation uses
 189 the PBLH derived from the Aircraft Meteorological Data Reports (AMDAR) at 54 sites across the
 190 CONUS to adjust the PBLH estimates as described in Li et al., (2023). We examine the effect of
 191 using the adjusted PBLH for simulations over the CONUS, Europe and East Asia. Table 1 shows
 192 the 3 simulation cases conducted over Maryland, Texas, Colorado, the CONUS, Europe and East
 193 Asia.

194 Table 1. Summary of GCHP Simulations

Name	Description
Base_12	12 km base
No Δ BL_12	12 km without PBLH modification
No Δ BL_55	55 km without PBLH modification

200 **2.5 Effective temperature of Pandora measurements**

201 The NO₂ cross section is temperature dependent with the magnitude of spectral features in a 294
 202 K NO₂ spectrum about 80% of those in 220 K NO₂ spectrum (Vandaele et al., 2002). Thus, the
 203 NO₂ columns fitted with a 220 K NO₂ spectrum are about 80% of those fitted with the 294 K NO₂
 204 spectrum. Prior studies have ~~identifies~~ identified biases in the Pandora total ozone column effective
 205 temperature driven by ~~variation~~ variations in seasonal temperature (Zhao et al., 2016; Herman et
 206 al., 2015). ~~We compare Pandora NO₂ effective temperatures with~~ To account for the ~~site-specific~~
 207 hourly changes in vertical variation of ~~hourly effective~~ column temperature, ~~we calculate simulated~~

208 NO₂ effective temperatures T_{eff} using the site-specific hourly GEOS-FP temperature profiles
209 (T)_{*i*} NO₂ cross section $\sigma(NO_2)_{i}$ and GCHP NO₂ vertical profiles $VC(NO_2)_i$ following equation
210 (1) of Herman et al. (2009):

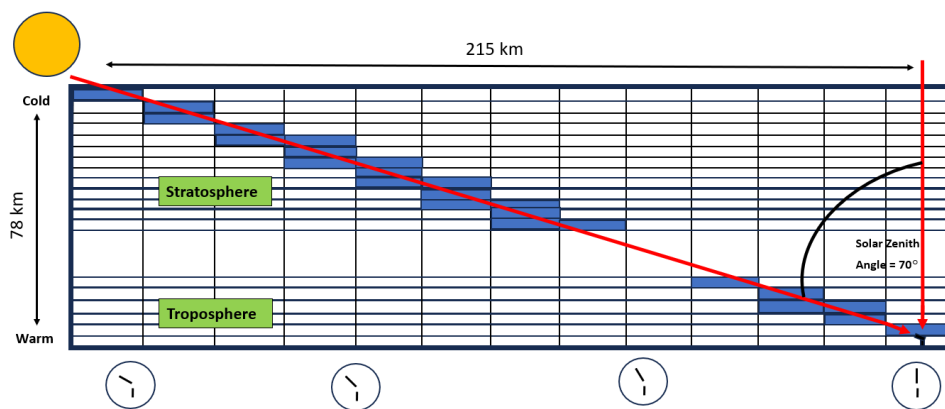
$$211 \quad T_{eff} = \frac{\sum_i^N (\sigma(NO_2)_i \cdot VC(NO_2)_i \cdot (T)_i)}{\sum_i^N (\sigma(NO_2)_i \cdot VC(NO_2)_i)} \quad (1)$$

212 The comparison between GCHP simulated and Pandora observed effective temperature is
213 discussed in sec 3.2.

214 **2.6 Local solar time along Pandora line-of-sight**

215 At observing scenarios with large solar zenith angles, the Pandora sun photometer observes
216 air masses with varying local solar time at different altitudes along the line-of-sight. This feature
217 is particularly noteworthy for comparing hourly Pandora observations with other measurements or
218 simulations. Figure 1 shows the sampling process of GCHP simulations along the line-of-sight of
219 the Pandora sun photometer. GCHP grid boxes are integrated along the viewing geometry of the
220 Pandora instrument to create a “staircase column” that accounts for the effects of local solar time
221 on the horizontal and vertical variation in NO₂ concentrations. The variation in local solar time is
222 most relevant near sunrise and sunset when the NO₂/NO_x ratios changeschange rapidly as
223 discussed in section 3.2. We correct the vertical columns reported by PGN to the local solar time
224 of the instrument by applying the ratio of integrated staircase columns to vertical columns.

Formatted: Indent: First line: 0.5"



225
 226 Figure 1. Configuration of integrating the GCHP grid boxes along the line-of-sight of the Pandora
 227 instrument. The shaded grid boxes represent the line-of-sight for the Pandora sun photometer at an inclined
 228 solar zenith angle. Clock faces indicate a change in local solar time.

229 **2.7 Ground based surface NO₂ measurements**

230 We use hourly NO₂ surface concentrations from the catalytic converter measurements over
 231 DISCOVER-AQ and PGN sites. Based on the approach of Lamsal et al., (2008) and Shah et al.,
 232 (2020), we correct the interference of organic nitrates and HNO₃ in the NO₂ measurements, using
 233 a correction factor derived from GCHP simulated site-specific NO₂, organic nitrates, and HNO₃
 234 mixing ratios. The correction for HNO₃ and organic nitrates reduced the summertime mean NO₂
 235 surface concentrations by 18% over DISCOVER-AQ sites and 23% over PGN sites.

236 **2.8 Normalized Bias**

237 We use normalized absolute bias or normalized bias (NB) to evaluate the simulations. The NB is
 238 calculated using the following equation-

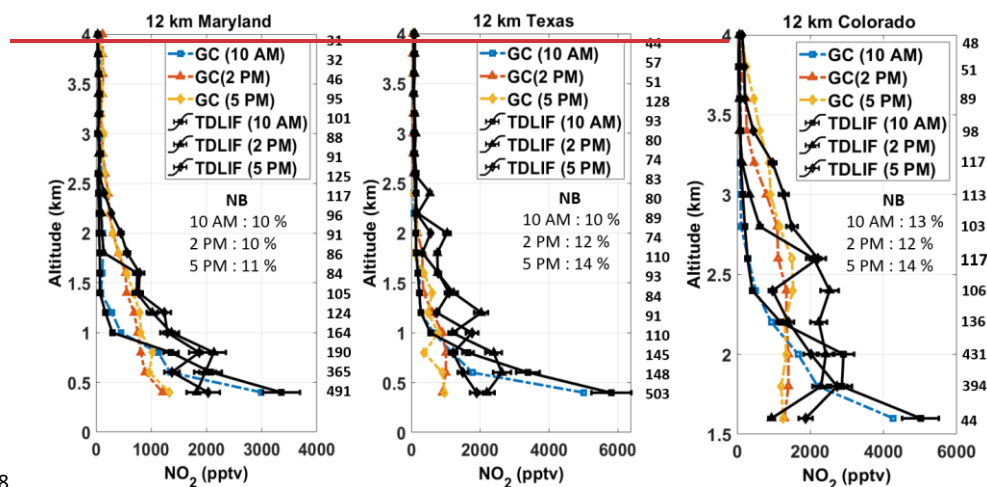
239
$$NB = \frac{\sum_{i=1}^N |S_i - O_i|}{\sum_{i=1}^N O_i} \times 100\% \quad \text{-----} \quad (2)$$

240 where, O_i is the observation and S_i is the corresponding simulated value, i refers to the index of
 241 the observation and N refers to the total number of observations.

242 3 Results and Discussion

243 3.1 Hourly variation of observed and simulated NO₂ vertical profiles

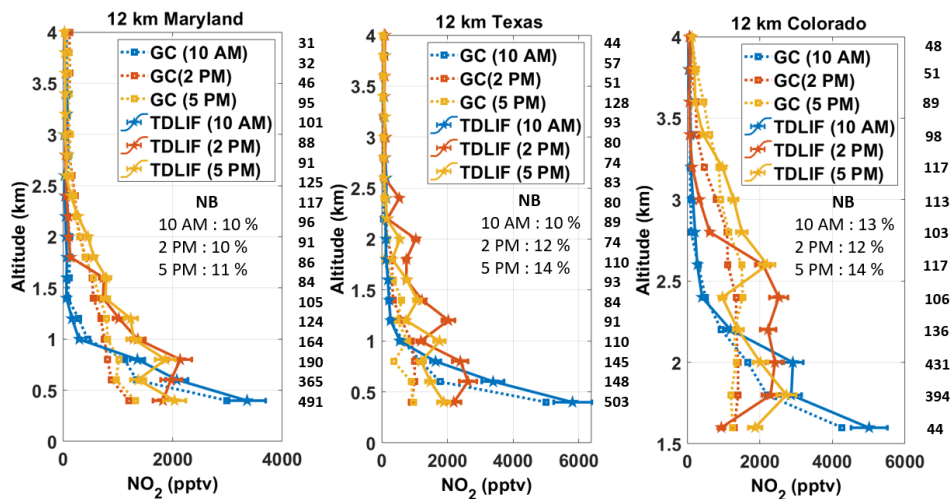
244 Figure 2 shows the hourly variation in the airborne TD-LIF measurements and simulated NO₂
 245 vertical profiles at 12 km resolution (Base_12) over Maryland, Texas and Colorado during the
 246 DISCOVER-AQ campaign. The measurements exhibit a pronounced maximum at 500 m at 10
 247 AM (squares) that diminishes by a factor of 2 in the afternoon as concentrations become more



249 **Figure 2: NO₂ vertical profiles from TD-LIF instrument aboard P-3B during the DISCOVER-AQ campaign**
 250 **over Maryland, Texas and Colorado. The black lines represent observations (square: 10 AM, triangle: 2**
 251 **PM, diamond: 5 PM). The colored lines represent 12 km GCHP simulated mixing ratios (blue: 10 AM,**
 252 **orange: 2 PM, yellow: 5 PM). The inset values in the boxes show the normalized biases (NBs) at 10 AM,**
 253 **2 PM, and 5 PM. The numbers on the right of each panel represent the number the observations associated**
 254 **with the corresponding altitude level. Error bars indicate standard errors in measurements.**

255 uniform below 1.5 km (triangles and diamonds), driven by the hourly variation in PBLH mixing
 256 from early morning to late afternoon. -For all three DISCOVER-AQ campaigns, the 12 km

257 simulated NO₂ mixing ratios (left panel) represent the vertical profile well with normalized bias
 258 (NB) below 16% at local times: 10 AM, 2 PM, and 5 PM. Differences tend to be larger within 1-
 259 2 km above ground level in the afternoon (2 PM and 5 PM local time), which integrates to a lower
 260 simulated partial column of 6×10^{14} molecules cm⁻². The simulated NO₂ vertical profiles at 12 km
 261 without PBLH modifications (No Δ ABL_12) are similar to those with the PBLH modification
 262 (Figure A3). Figure A4 shows the 55 km simulated NO₂ vertical profiles (No Δ ABL_55). The 55 km
 263 GCHP simulations have increased NB by a factor of 2, as compared to ~~at~~-12 km. Overall, the NO₂
 264 vertical profile exhibits greater consistency with observations at 12 km than at 55 km by better
 265 resolving

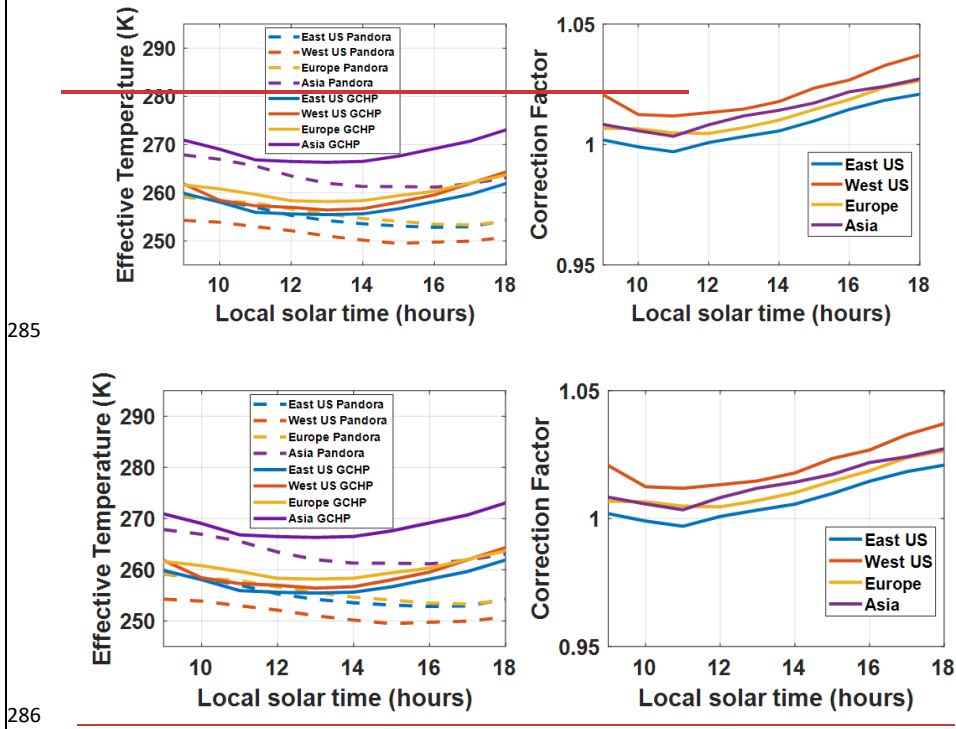


266
 267 Figure 2: NO₂ vertical profiles from TD-LIF instrument aboard P-3B during the DISCOVER-AQ campaign
 268 over Maryland, Texas, and Colorado. The colored solid lines with pentagram markers represent
 269 observations. The dotted colored lines with square markers represent 12 km GCHP simulated mixing ratios.
 270 The inset values in the boxes show the normalized biases (NBs) at 10 AM, 2 PM, and 5 PM. The numbers
 271 on the right of each panel represent the number the observations associated with the corresponding altitude
 272 level. Error bars indicate standard errors in measurements.

273 -the heterogeneous conditions along the aircraft flight tracks.

274 **3.2 Corrections to Pandora Effective Temperature**

275 The left panel in Figure 3 shows the Pandora and simulated mean hourly effective temperature of
276 the NO₂ columns over all PGN sites during June-August as inferred using hourly GEOS-FP
277 temperature profiles and GCHP NO₂ vertical profiles. The Pandora effective temperatures exhibit
278 weak hourly variation with a warmer temperature at the Asian sites where boundary layer NO₂
279 concentrations are typically higher than in the US and Europe. The GCHP simulated effective
280 temperature is also warmer for Asian sites, however, the effective temperature is lower during the
281 early afternoon when near-surface NO₂ concentrations tend to be minimum such that the
282 stratospheric NO₂ that makes a larger fractional contribution to the total column. The simulated
283 effective temperature further deviates from the Pandora effective temperature with an increase
284 toward sunrise and sunset with increasing near-surface NO₂ fraction. The corresponding correction



287 Figure 3. Hourly variation of the total NO₂ column mean effective temperature across all PGN sites (left
 288 panel) and the corresponding correction factors (right panel).

289 ~~temperature profiles and GCHP NO₂-vertical profiles. The simulated effective temperature is~~
 290 ~~lowest in early afternoon when near surface NO₂ concentrations are minimum such that~~
 291 ~~stratospheric NO₂ makes a larger fractional contribution to the total column. The simulated~~
 292 ~~effective temperature deviates from the Pandora effective temperature with an increase toward~~
 293 ~~sunrise and sunset with increasing near surface NO₂ fraction. factor (CF) for hourly variation in~~
 294 ~~the effective temperature is calculated as:~~

295 ~~_____~~
$$CF = 1 + \left(\frac{1}{0.8} - 1\right) \times \frac{(T_{eff}(GCHP(hour)) - T_{eff}(Pandora(hour)))}{294 - 220}$$
 ~~The corresponding~~

296 ~~correction factor (CF) for hourly variation in the effective temperature calculated as:~~

297

$$CF = 1 +$$

298

$$\frac{0.2(T_{eff}(GCHP(hour)) - T_{eff}(Pandora(hour)))}{294 - 220} \quad (2(3))$$

299

The factor of $(\frac{1}{0.8} - 1)$ reflects the difference between the NO₂ columns fitted with a 220 K NO₂

300

spectrum that are about 80% of those fitted with a 294 K NO₂ spectrum. The CF for the Pandora

301

NO₂ columns increases toward sunrise and sunset due to the increased effective temperature,

302

reflecting the greater abundance of NO₂ molecules observed per unit absorption. We apply site-

303

specific CFs across all Pandora observations.

Formatted: Justified

304

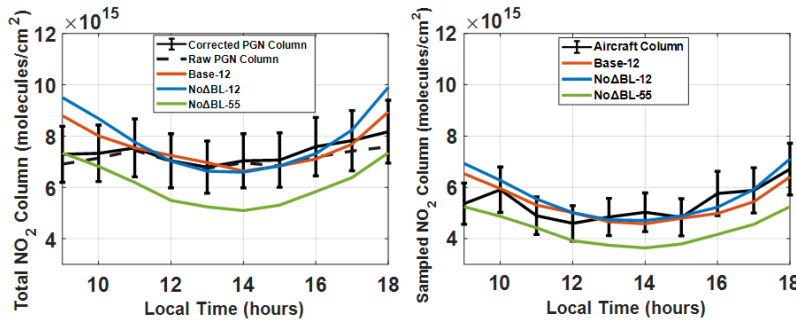
3.3 Hourly variation of observed and simulated NO₂ VCDs

305

Figure 4 (left) shows the mean hourly daytime Pandora vertical NO₂ columns summarized

306

from the summertime DISCOVER-AQ campaign measurements. The raw Pandora NO₂ columns



307

308

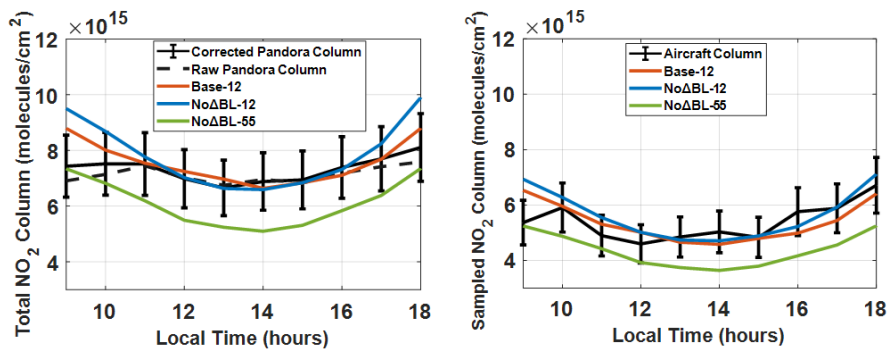
from the summertime DISCOVER-AQ campaign measurements. The raw Pandora NO₂ columns

310

exhibit weak hourly variation of 8×10^{14} molecules cm⁻² (within 10% of the daytime mean) that

311

is inconsistent with the aircraft measurements that indicate total columns in the morning and



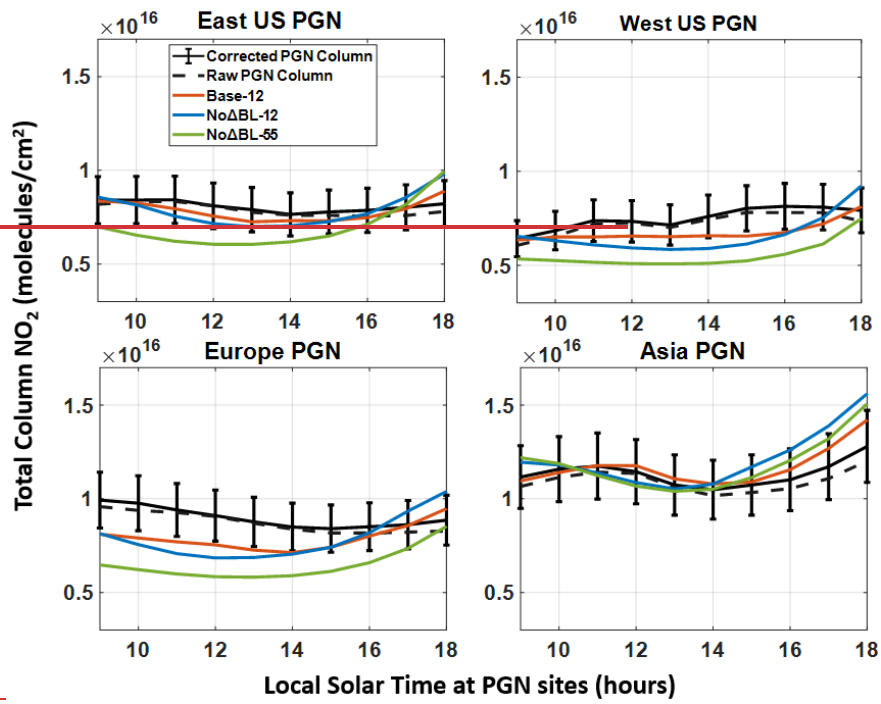
312
 313 Figure 4. The left panel shows the total NO₂ vertical columns from corrected DISCOVER-AQ Pandora
 314 columns (black), raw DISCOVER-AQ Pandora columns (black dotted), the 12 km base case simulation
 315 with staircase columns (red), 12 km without modified PBLH (blue) and 55 km without modified PBLH
 316 (green), during the DISCOVER-AQ campaigns over Maryland (2011), Texas (2013) and Colorado (2014).
 317 The corrected PGNPandora columns account for the hourly variation in the effective temperature and the
 318 local solar time along the line-of-sight. The right panel shows sampled aircraft and simulated partial
 319 columns (300 m A.G.L - 4 km A.G.L). Error bars indicate standard error.

320
 321 ~~exhibit weak hourly variation of 8×10^{14} molecules cm^{-2} (within 10% of the daytime mean) that~~
 322 ~~is inconsistent with the aircraft measurements that indicate total columns in the morning and~~
 323 evening of about 1.5×10^{15} molecules cm^{-2} greater than afternoon. The corrected Pandora
 324 measurements that account for hourly variation in effective temperature and local solar time along
 325 line-of-sight exhibit greater NO₂ columns in morning and evening by about 1.3×10^{15} molecules
 326 cm^{-2} , similar to the aircraft measurements. Since the Pandora instruments track the sun, viewing
 327 stratospheric air masses 100 - 200 km away from the measurement station to the East in the
 328 morning and to the West in the evening, the local solar time of stratospheric NO₂ observed by
 329 Pandora instruments near sunrise and sunset is systematically shifted by about 5-10 mins towards
 330 noon. This shift can be particularly important during sunrise and sunset when NO₂ columns in the
 331 stratosphere undergo a pronounced increase driven by an increasing NO₂/NO_x ratio (Figure A5).
 332 The 12 km simulated vertical columns generally represent the corrected Pandora observed columns
 333 with an NB of 10%. Excluding the PBLH modification would have increased the NB to 13%.

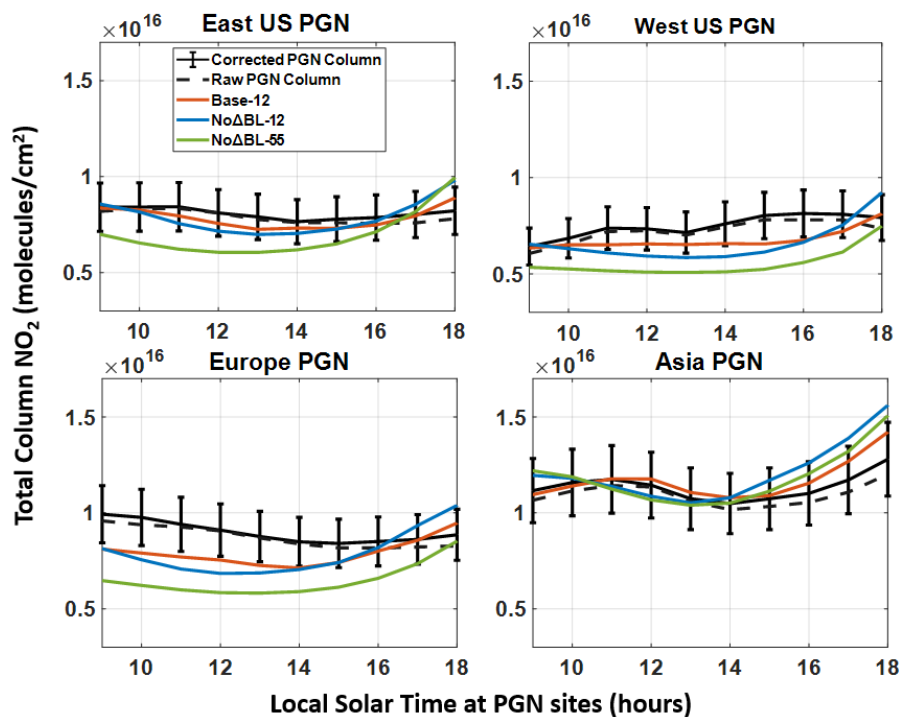
334 Using a coarser 55 km simulation would have further degraded the agreement with an NB of 19%.

335 We sample the GCHP simulated NO₂ columns between 300 m and 4 km to compare with the
336 aircraft columns (right panel). The hourly variation of partial NO₂ columns over 300 m to 4 km
337 AGL from aircraft observations exhibits a distinct increase in morning and evening and are well
338 represented by the 12 km base case simulation (NB = 13%). Similar to our analysis for Pandora
339 sites, excluding the PBLH modification and coarsening the simulation to 55 km degrades the
340 performance (NB = 15% and 25%) versus aircraft columns.

341 Figure 5 extends our analysis to all PGN sites across the CONUS, Europe and East Asia. Raw
342 measurements across all regions exhibit weak hourly variation. The correction for effective
343 temperature and local solar time along the Pandora line-of-site increases the mean NO₂ columns
344 in the morning and evening by about 6×10^{14} molecules cm⁻² across all regions. The base case
345 simulation generally reproduces measurements with NB of 9% for the eastern US, 14% for the
346 western US, 15% for ~~the~~ Europe and 21% for east Asia sites. Excluding the PBLH correction
347 would have increased the NB (eastern US: 12%, western US: 18%, Europe: 18%, and eastern
348 Asia: 26%) with the largest change in Asia. Excluding the PBLH correction yields a higher daytime
349 PBLH resulting in increased chemical lifetime of NO_x, reduced NO₂ dry deposition rates and
350 increased NO₂/NO_x ratio during afternoon and evening (Figure A6), thus leading to an hourly
351 variation that deviates from the Pandora observations. Coarser resolution generally further
352 increases the bias, reflecting resolution effects discussed in the next section. The increase of the
353 simulated total NO₂ columns between 3-6 PM across all PGN sites reflects an increase in the
354 NO₂/NO_x ratio throughout the column, driven by a reduction in HO_x (Figure A7).



355



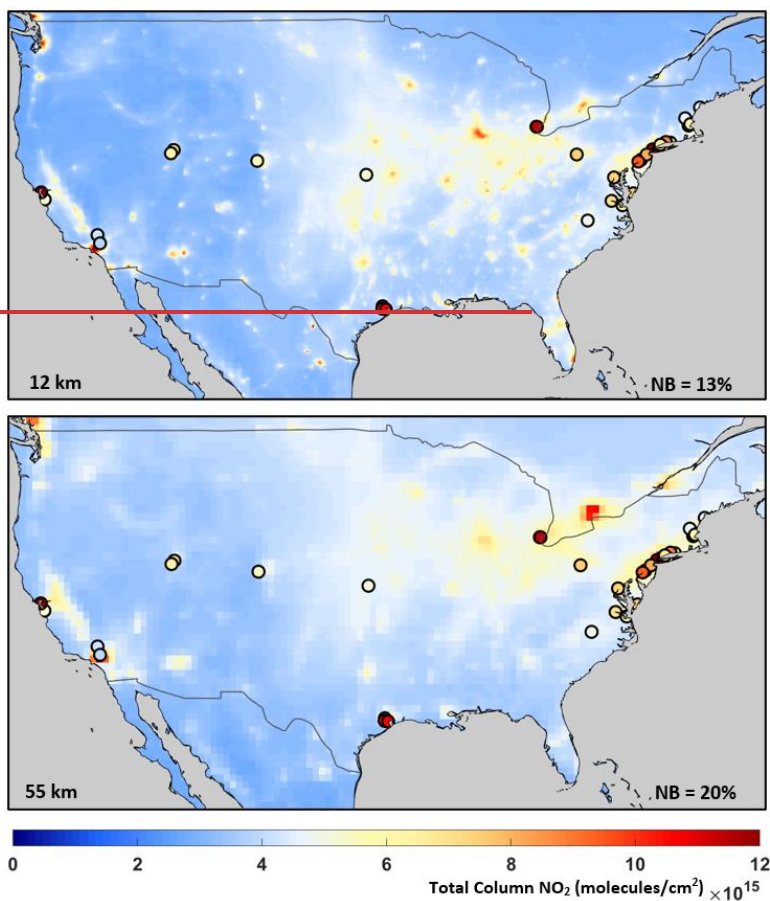
356

357 Figure 5. The total NO₂ vertical columns from corrected Pandora columns (black), raw Pandora columns
 358 (black dotted), the 12 km base case simulation with staircase columns (red), 12 km without modified PBLH
 359 (blue) and 55 km without modified PBLH (green) sampled over PGN sites for the summer months of June-
 360 July-August in 2019. Error bars indicate standard error.

361 ~~from the Pandora observations. Coarser resolution generally further increased 3.4 the bias,~~
 362 ~~reflecting resolution effects discussed in the next section. The increase of the simulated total NO₂~~
 363 ~~columns between 3–6 PM across all PGN sites reflects an increase in the NO₂/NO_x ratio throughout~~
 364 ~~the column, driven by a reduction in HO_x (Figure A7).~~

365 3.3 Simulated total NO₂ columns

366 Figure 6 shows the 12 km and 55 km simulated total NO₂ columns, for the summer months of
 367 June-July-August in 2019, between 9 AM and 6 PM (local solar time) over the CONUS. The

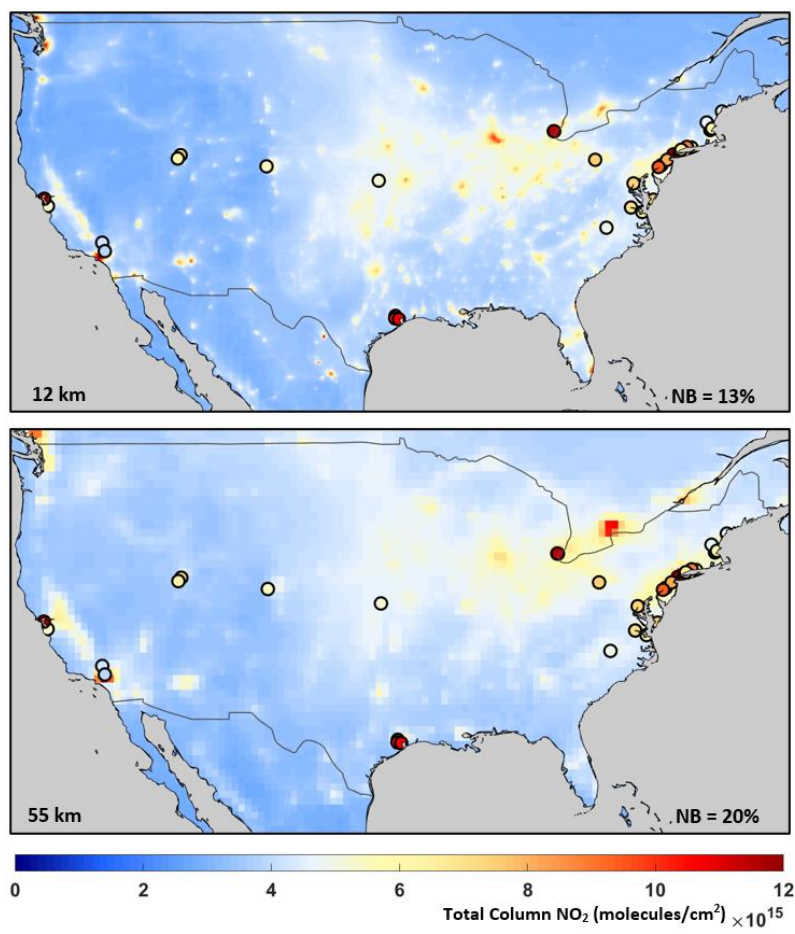


368
 369 ~~Figure 6. Simulated NO₂ total columns at 12 km (panel A) and 55 km (panel B) horizontal resolutions for~~
 370 ~~the three month average of June July August 2019 over domains where PGN monitors were available~~
 371 ~~between 9 AM – 6 PM local solar time. The solid circles represent the PGN mean total columns between~~
 372 ~~9 AM – 6 PM local solar time for PGN sites in CONUS (31)~~

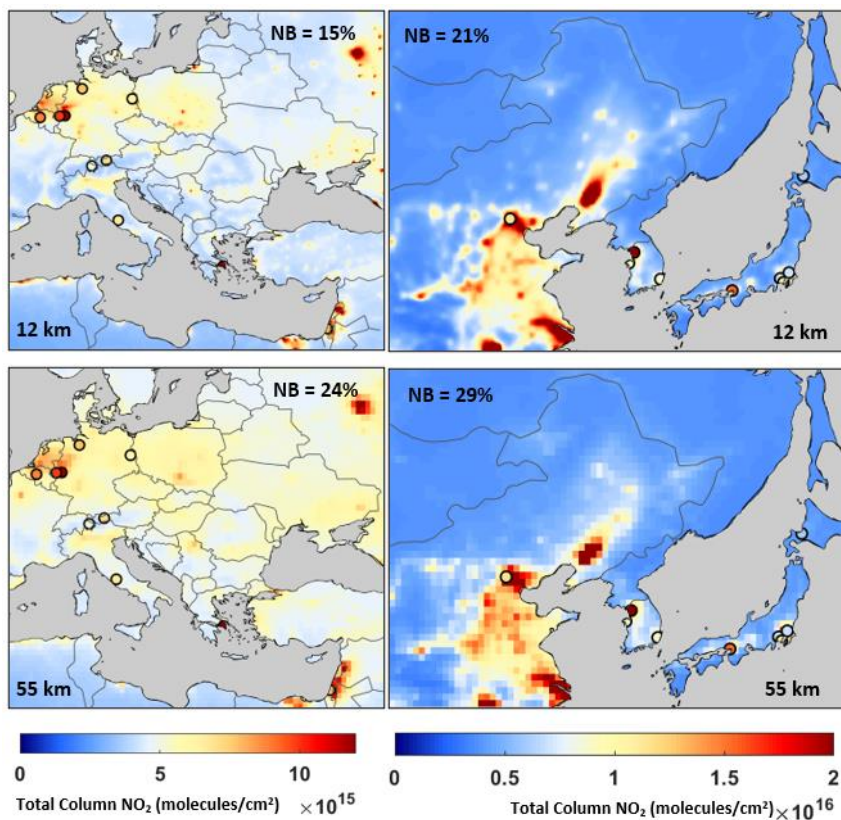
373 overlaid circles show the PGN mean total NO₂ columns. The 12 km simulated NO₂ columns
 374 exhibit greater heterogeneity and better consistency with PGN observed columns (NB = 13%) as
 375 compared to the 55 km simulated NO₂ columns (NB = 20%). This is primarily driven by better
 376 representation of emission and chemical processes at fine resolution (Zhang et al., 2023; Li et al.,

377 2023a). Emissions at these sites are dominated by the transportation sector (Table A3). [Figure 7](#)
378 [shows the total NO₂ columns from PGN, 12 km and 55 km for the summer months of June July](#)
379 [Figure 7.](#)

Formatted: Font: 11 pt



380
381 [Figure 6. Simulated NO₂ total columns at 12 km \(panel A\) and 55 km \(panel B\) horizontal resolutions for](#)
382 [the three-month average of June-July-August 2019 over domains where PGN monitors were available](#)
383 [between 9 AM – 6 PM local solar time. The solid circles represent the PGN mean total columns between](#)
384 [9 AM – 6 PM local solar time for PGN sites in CONUS \(31\)](#)



385

386 Figure 7. Simulated NO₂ total columns at 12 km (panel C and D) and 55 km (panel E and F) horizontal
 387 resolutions for the three-month average of June-July-August 2019 over domains where PGN monitors were
 388 available between 9 AM – 6 PM local solar time. The solid circles represent the PGN mean total columns
 389 between 9 AM – 6 PM local solar time for the PGN sites in Europe (10) and Asia (9).

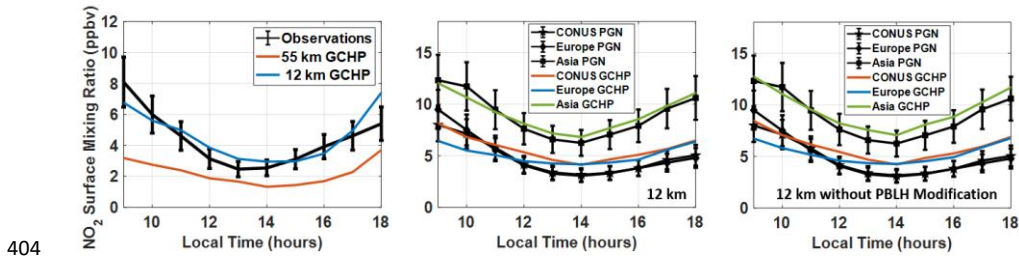
390 shows the total NO₂ columns from PGN, 12 km simulation and 55 km simulation for the summer
 391 months of June-July- August in 2019, between 9 AM and 6 PM local solar time over Europe and
 392 Europe and East Asia. We find enhanced NO₂ vertical columns over urban areas in western Europe, eastern
 393 China, Japan and the Korean peninsula. The 12 km simulated NO₂ columns exhibit more resolved
 394 combustion features and better agreement with Pandora observed columns for Europe (NB = 15%)

395 and east Asia (NB = 17%) as compared to the 55 km simulated NO₂ columns for Europe (NB
 396 =24%) and east Asia (NB =29%).
 397 24%) and east Asia (NB = 29%).

Formatted: Font: 12 pt

398 **3.45 Hourly variation of observed and simulated surface NO₂ concentrations**

399 Figure 8 shows the hourly variation in surface NO₂ mixing ratios from the corrected in situ
 400 measurements and 12 km simulations over Maryland, Texas and Colorado. Measured NO₂ mixing
 401 ratios are greater in morning and evening than in afternoon as expected from the mixed layer
 402 growth and shorter NO_x lifetime in afternoon. Observed NO₂ surface concentrations over PGN
 403 sites in Asia show enhancement at evening hours (5-6 PM) as compared to PGN sites elsewhere.



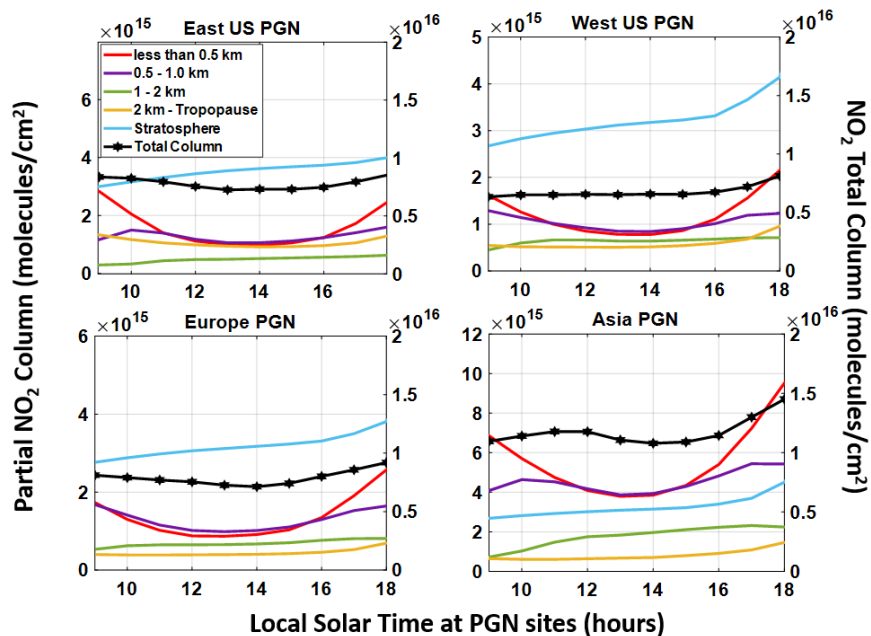
404 Figure 8. The left panel shows the hourly variation of corrected surface NO₂ mixing ratios from
 405 observations during the DISCOVER-AQ campaign. The middle and right panels show the hourly variation
 406 of observed and 12 km PBLH modified and 12 km simulated surface NO₂ mixing ratios averaged over the
 407 PGN sites with and without PBLH modification respectively. Error bars indicate standard error.

408 The measurements are better represented at 12 km (NB = 21%) than at 55 km (NB = 63%) by
 409 better resolving high NO_x emissions near measurement sites. Both Base_12 and NoΔBL_12
 410 simulated NO₂ concentrations generally represent the observations well with NB = 18% (Base_12)
 411 and NB = 20% (NoΔBL_12), across all PGN sites.

Formatted: Font: 11 pt

412 =20% (NoΔBL_12), across all PGN sites.
 413 =20% (NoΔBL_12), across all PGN sites.

414 **3.56** Hourly variation of layer contributions to simulated total NO₂ ~~staircase~~ columns
 415 WeGiven the overall skill of the 12 km simulations in representing the Pandora, aircraft, and
 416 surface NO₂ we proceed to apply the 12 km simulations to understand how the simulated NO₂
 417 vertical profile affects the simulated NO₂ column to surface relationship. Figure 9 shows the hourly
 418 variation of simulated contributions to the NO₂ total columns (Base_12) from different vertical
 419 layers for multiple regions. In all four regions, within the troposphere, the layer below 0.5 km is
 420 the largest contributor at 9 AM with a diminishing contribution into the afternoon associated with
 421 mixed layer growth and followed by an increasing contribution towards evening. The contribution
 422 from layers between 0.5 km and the tropopause



423
 424 Figure 9. The simulated absolute contribution of NO₂ columns at different hours of the day averaged over
 425 the summer months of June-July-August for 2019 for PGN sites over the eastern US, western US, Europe,
 426 and eastern Asia. The colored lines resemble the absolute concentrations from different sections of the
 427 column. The black line (hexagon) represents the total NO₂ column. The right y-axis (specifically for the
 428 total NO₂ column representing the black marked line) shows the total columns of NO₂.

429 from layers between 0.5 km and the tropopause has weaker variation contributing to the overall
430 weaker variation in total columns. Fractional layer contributions are shown in Figure A8.
431 Fractional hourly variation of the layers above 0.5 km exhibits a compensating inverse behavior,
432 with a pronounced variation in the stratospheric fraction. Contributions from the free troposphere
433 are relatively high for the eastern US reflecting the lightning contribution (Shah et al., 2023; Dang
434 et al., 2023). Over Asia the fractional contribution below 0.5 km is the highest (26% - 42%)
435 reflecting major surface contributions. Overall, we find that for all four regions, the hourly
436 variation in the total column reflects hourly variation below 500 m, dampened by greater column
437 contributions above 500 m that dominate the total column.

438 **Conclusion**

439 We applied ~~the GCHP model~~ to investigate the hourly variation of summertime NO₂ columns and
440 surface concentrations by interpreting DISCOVER-AQ aircraft and ground-based measurements
441 over Maryland, Texas, Colorado and PGN measurements over the CONUS, Europe, and eastern
442 Asia. We corrected the hourly variation in Pandora observations for the effects of temperature on
443 the NO₂ cross section and the local solar time along the Pandora line-of-sight. The site-specific
444 effective temperature correction factors typically increase the hourly variation of the Pandora
445 observed columns over DISCOVER_AQ sites (3.5% from the daytime mean) and PGN sites (4%
446 from the daytime mean). Near sunrise and sunset, differences in local solar time observed by
447 Pandora in the stratosphere versus the measurement site reflect displacement of 5-10 mins in local
448 solar time toward noon which is relevant in the stratosphere near sunrise and sunset when the
449 NO₂/NO_x ratio is varying rapidly. These corrections to the Pandora measurements improve their
450 consistency with the hourly variation in the NO₂ columns inferred from DISCOVER-AQ aircraft
451 measurements. We find that ~~the~~ fine scale simulations at 12 km better represent the NO₂ vertical

452 profile measured by aircraft, reducing the NB from 23% to 16% as compared to ~~the~~ simulations at
453 a moderate resolution of 55 km. Simulations at fine resolution (~12 km) of vertical columns along
454 the line-of-sight of Pandora instruments ~~agree better~~ have lower NB with Pandora sun photometers
455 at DISCOVER-AQ sites (10%), and across the eastern US (9%), western US (14%), Europe (15%)
456 and Asia (21%) as compared to moderate resolution (55 km). Fine resolution represents
457 atmospheric physical and chemical processes with greater accuracy. Excluding the effects of
458 model resolution, and the PBLH modification increases the NB to 21% across DISCOVER-AQ
459 sites (over Maryland, Texas and Colorado) and increases the NB at PGN sites over the eastern US
460 (17%), western US (~~24%~~ 21%), Europe (24%) and east Asia (29%). Adjusting the PBLH to
461 represent observations ~~improved~~ improves the daytime variation in NO₂/NO_x ratios by increasing
462 the NO₂/NO_x ratio in midday and decreasing the NO₂/NO_x ratio in the afternoon and evening.

463 ~~We use the simulated columns~~ Given the overall skill of the 12 km GCHP simulations in
464 representing the corrected Pandora, aircraft, and surface NO₂ measurements, we apply them to
465 derive the hourly contribution of vertical layers to the total tropospheric columns. We find weaker
466 hourly variation in total NO₂ columns than in the lowest 500 m where NO₂ concentrations are
467 greater in morning and evening than midday, while the residual tropospheric column above 500 m
468 dominates the total column with weaker variability. Thus, the weak hourly variation in the column
469 reflects fractional contributions from NO₂ below and above 500 m. ~~Future work should~~ Despite the
470 skill of the 12 km simulations in representing the Pandora column measurements, there appears to
471 be greater hourly variation in the simulation, the aircraft measurements, and the surface
472 measurements than in the Pandora observations. Future work should continue to understand this
473 relationship. Future work should also leverage the information developed here to test the

Formatted: Indent: First line: 0"

474 performance of surface NO₂ concentrations inferred from the geostationary constellation
475 ~~versus~~against ground-based measurements.

476 **Code and Data Availability**

477 GEOS-Chem 14.1.1 along with GCHP code is available for download at
478 <https://github.com/geoschem/GCHP.git>. The PGN data is available at [https://data.pandonia-](https://data.pandonia-global-network.org/)
479 [global-network.org/](https://data.pandonia-global-network.org/). The DISCOVER-AQ aircraft and Pandora data are available here:
480 <https://asdc.larc.nasa.gov/project/DISCOVER-AQ>. For hourly simulated NO₂ datasets please
481 contact the author (deepangsuchatterjee@wustl.edu; deepangsuchatterjee@gmail.com)

482 **Author contributions**

483 The manuscript was written using contributions from all authors. The conceptualization was
484 initialized by DC and RVM. The methodology was developed by DC and RVM .DC conducted
485 the model simulations. DC conducted the data analysis with help from CL,DZ,HZ,LL,DH,RC. JC
486 conducted the DISCOVER-AQ campaign. AC manages the PGN datasets. DC and RVM wrote
487 the original draft. All authors have reviewed, edited and given approval to the final version of the
488 ~~manuscript.~~
489 manuscript.

490 **Competing interests**

491 The contact author has declared that neither they nor their co-authors have any competing interests.

492 **Acknowledgments**

494 This work has been supported by the NASA Grant 80NSSC21K1343 and 80NSSC21K0508 and
495 NSF Grant 2244984. We thank the GEOS-Chem support team for maintaining the model used in
496 this work.

497 **Reference**

- 498 Al-Saadi, J., Kim, J., Lambert, J.-C., Veihelmann, B., and Chance, K.: Geostationary Satellite
499 Constellation for Observing Global Air Quality : Geophysical Validation Needs, 2017.
- 500 Anenberg, S. C., Henze, D. K., Tinney, V., Kinney, P. L., Raich, W., Fann, N., Malley, C. S., Roman, H.,
501 Lamsal, L., Duncan, B., Martin, R. V., van Donkelaar, A., Brauer, M., Doherty, R., Jonson, J. E., Davila,
502 Y., Sudo, K., and Kuylenstierna, J. C. I.: Estimates of the global burden of ambient PM_{2.5}, ozone, and
503 NO₂ on asthma incidence and emergency room visits, *Environ. Health Perspect.*, 126, 1–14,
504 <https://doi.org/10.1289/EHP3766>, 2018.
- 505 Anenberg, S. C., Mohegh, A., Goldberg, D. L., Kerr, G. H., Brauer, M., Burkart, K., Hystad, P., Larkin,
506 A., Wozniak, S., and Lamsal, L.: Long-term trends in urban NO₂ concentrations and associated paediatric
507 asthma incidence: estimates from global datasets, *Lancet Planet. Heal.*, 6, e49–e58,
508 [https://doi.org/10.1016/S2542-5196\(21\)00255-2](https://doi.org/10.1016/S2542-5196(21)00255-2), 2022.
- 509 Bates, K. H. and Jacob, D. J.: A new model mechanism for atmospheric oxidation of isoprene: Global
510 effects on oxidants, nitrogen oxides, organic products, and secondary organic aerosol, *Atmos. Chem.*
511 *Phys.*, 19, 9613–9640, <https://doi.org/10.5194/acp-19-9613-2019>, 2019.
- 512 Bates, K. H., Jacob, D. J., Li, K., Ivatt, P. D., Evans, M. J., Yan, Y., and Lin, J.: Development and
513 evaluation of a new compact mechanism for aromatic oxidation in atmospheric models, *Atmos. Chem.*
514 *Phys.*, 21, 18351–18374, <https://doi.org/10.5194/acp-21-18351-2021>, 2021.
- 515 Bauer, S. E., Koch, D., Unger, N., Metzger, S. M., Shindell, D. T., and Streets, D. G.: Nitrate aerosols
516 today and in 2030: A global simulation including aerosols and tropospheric ozone, *Atmos. Chem. Phys.*,
517 7, 5043–5059, <https://doi.org/10.5194/acp-7-5043-2007>, 2007.
- 518 Belinha, J.: Manual for FEMAS Manual for FEMAS, 1–83, 2016.
- 519 Bindle, L., Martin, R. V., Cooper, M. J., Lundgren, E. W., Eastham, S. D., Auer, B. M., Clune, T. L.,
520 Weng, H., Lin, J., Murray, L. T., Meng, J., Keller, C. A., Putman, W. M., Pawson, S., and Jacob, D. J.:
521 Grid-stretching capability for the GEOS-Chem 13.0.0 atmospheric chemistry model, *Geosci. Model Dev.*,
522 14, 5977–5997, <https://doi.org/10.5194/GMD-14-5977-2021>, 2021.
- 523 Burnett, R. T., Stieb, D., Brook, J. R., Cakmak, S., Dales, R., Raizenne, M., Vincent, R., and Dann, T.:
524 Associations between Short-Term Changes in Nitrogen Dioxide and Mortality in Canadian Cities, *Arch.*
525 *Environ. Heal. An Int. J.*, 59, 228–236, <https://doi.org/10.3200/AEOH.59.5.228-236>, 2004.
- 526 Cede (2021) [https://www.pandonia-global-](https://www.pandonia-global-network.org/wpcontent/uploads/2021/09/BlickSoftwareSuite_Manual_v1-8-4.pdf)
527 [network.org/wpcontent/uploads/2021/09/BlickSoftwareSuite_Manual_v1-8-4.pdf](https://www.pandonia-global-network.org/wpcontent/uploads/2021/09/BlickSoftwareSuite_Manual_v1-8-4.pdf)
- 528 Choi, S., Lamsal, L. N., Follette-Cook, M., Joiner, J., Krotkov, N. A., Swartz, W. H., Pickering, K. E.,
529 Loughner, C. P., Appel, W., Pfister, G., Saide, P. E., Cohen, R. C., Weinheimer, A. J., and Herman, J. R.:
530 Assessment of NO₂ observations during DISCOVER-AQ and KORUS-AQ field campaigns, *Atmos.*
531 *Meas. Tech.*, 13, 2523–2546, <https://doi.org/10.5194/amt-13-2523-2020>, 2020.
- 532 Cooper, M. J., Martin, R. V., Hammer, M. S., Levelt, P. F., Veeffkind, P., Lamsal, L. N., Krotkov, N. A.,
533 Brook, J. R., and McLinden, C. A.: Global fine-scale changes in ambient NO₂ during COVID-19
534 lockdowns, *Nature*, 601, 380–387, <https://doi.org/10.1038/s41586-021-04229-0>, 2022.
- 535 Crawford, J. H., Ahn, J., Al-saadi, J., Chang, L., Emmons, L. K., Kim, J., Lee, G., Park, J., Park, R. J.,
536 Woo, J. H., Song, C., Hong, J., Hong, Y., Lefer, B. L., Lee, M., Lee, T., Kim, S., Min, K., Yum, S. S.,
537 Shin, H. J., Kim, Y., Choi, J., Park, J., Szykman, J. J., Long, R. W., Jordan, C. E., Simpson, I. J., Fried,

538 A., Dibb, J. E., Cho, S., and Kim, Y. P.: The Korea-United States Air Quality (KORUS-AQ) field study,
539 1–27, 2021.

540 Crippa, M., Guizzardi, D., Muntean, M., Schaaf, E., Dentener, F., Van Aardenne, J. A., Monni, S.,
541 Doering, U., Olivier, J. G. J., Pagliari, V., and Janssens-Maenhout, G.: Gridded emissions of air pollutants
542 for the period 1970-2012 within EDGAR v4.3.2, *Earth Syst. Sci. Data*, 10, 1987–2013,
543 <https://doi.org/10.5194/essd-10-1987-2018>, 2018.

544 Dang, R., Jacob, D. J., Shah, V., Eastham, S. D., Fritz, T. M., Mickley, L. J., Liu, T., Wang, Y., and
545 Wang, J.: Background nitrogen dioxide (NO₂) over the United States and its implications for satellite
546 observations and trends: effects of nitrate photolysis, aircraft, and open fires, *Atmos. Chem. Phys.*, 23,
547 6271–6284, <https://doi.org/10.5194/acp-23-6271-2023>, 2023.

548 David, L. M. and Nair, P. R.: Diurnal and seasonal variability of surface ozone and NO_x at a tropical
549 coastal site: Association with mesoscale and synoptic meteorological conditions, *J. Geophys. Res.*, 116,
550 1–16, <https://doi.org/10.1029/2010jd015076>, 2011.

551 Day, D. A., Wooldridge, P. J., Dillon, M. B., Thornton, J. A., and Cohen, R. C.: A thermal dissociation
552 laser-induced fluorescence instrument for in situ detection NO₂, peroxy nitrates, alkyl nitrates, and
553 HNO₃, *J. Geophys. Res. Atmos.*, 107, <https://doi.org/10.1029/2001jd000779>, 2002.

554 Day, D. A., Farmer, D. K., Goldstein, A. H., Wooldridge, P. J., Minejima, C., and Cohen, R. C.:
555 Observations of NO_x, α PNs, α ANs, and HNO₃ at a rural site in the California Sierra Nevada Mountains:
556 Summertime diurnal cycles, *Atmos. Chem. Phys.*, 9, 4879–4896, [https://doi.org/10.5194/acp-9-4879-](https://doi.org/10.5194/acp-9-4879-2009)
557 2009, 2009.

558 Duncan, B. N., Yoshida, Y., De Foy, B., Lamsal, L. N., Streets, D. G., Lu, Z., Pickering, K. E., and
559 Krotkov, N. A.: The observed response of Ozone Monitoring Instrument (OMI) NO₂ columns to NO_x
560 emission controls on power plants in the United States: 2005-2011, *Atmos. Environ.*, 81, 102–111,
561 <https://doi.org/10.1016/j.atmosenv.2013.08.068>, 2013.

562 Eastham, S. D., Weisenstein, D. K., and Barrett, S. R. H.: Development and evaluation of the unified
563 tropospheric-stratospheric chemistry extension (UCX) for the global chemistry-transport model GEOS-
564 Chem, *Atmos. Environ.*, 89, 52–63, <https://doi.org/10.1016/j.atmosenv.2014.02.001>, 2014.

565 Eastham, S. D., Long, M. S., Keller, C. A., Lundgren, E., Yantosca, R. M., Zhuang, J., Li, C., Lee, C. J.,
566 Yannetti, M., Auer, B. M., Clune, T. L., Kouatchou, J., Putman, W. M., Thompson, M. A., Trayanov, A.
567 L., Molod, A. M., Martin, R. V., and Jacob, D. J.: GEOS-Chem high performance (GCHP v11-02c): A
568 next-generation implementation of the GEOS-Chem chemical transport model for massively parallel
569 applications, *Geosci. Model Dev.*, 11, 2941–2953, <https://doi.org/10.5194/GMD-11-2941-2018>, 2018.

570 Flynn, C. M., Pickering, K. E., Crawford, J. H., Lamsal, L., Krotkov, N., Herman, J., Weinheimer, A.,
571 Chen, G., Liu, X., Szykman, J., Tsay, S. C., Loughner, C., Hains, J., Lee, P., Dickerson, R. R., Stehr, J.
572 W., and Brent, L.: Relationship between column-density and surface mixing ratio: Statistical analysis of
573 O₃ and NO₂ data from the July 2011 Maryland DISCOVER-AQ mission, *Atmos. Environ.*, 92, 429–441,
574 <https://doi.org/10.1016/j.atmosenv.2014.04.041>, 2014.

575 Fountoukis, C. and Nenes, A.: ISORROPIAII: A computationally efficient thermodynamic equilibrium
576 model for K⁺-Ca²⁺-Mg²⁺-NH₄⁺-Na⁺-SO₄²⁻-NO₃⁻-Cl⁻-H₂O aerosols, *Atmos. Chem. Phys.*, 7, 4639–
577 4659, <https://doi.org/10.5194/ACP-7-4639-2007>, 2007.

578 Geddes, J. A. and Martin, R. V: Global deposition of total reactive nitrogen oxides from, *Atmos. Chem.*
579 *Phys.*, 17, 10071–10091, 2017.

580 Ghude, S. D., Karumuri, R. K., Jena, C., Kulkarni, R., Pfister, G. G., Sajjan, V. S., Pithani, P., Debnath,

581 S., Kumar, R., Upendra, B., Kulkarni, S. H., Lal, D. M., Vander A, R. J., and Mahajan, A. S.: What is
582 driving the diurnal variation in tropospheric NO₂ columns over a cluster of high emission thermal power
583 plants in India?, *Atmos. Environ.*, *X*, 5, 100058, <https://doi.org/10.1016/j.aeaoa.2019.100058>, 2020.

584 Herman, J., Cede, A., Spinei, E., Mount, G., Tzortziou, M., and Abuhassan, N.: NO₂ column amounts
585 from ground-based Pandora and MFDOAS spectrometers using the direct-sun DOAS technique:
586 Intercomparisons and application to OMI validation, *J. Geophys. Res. Atmos.*, *114*, 1–20,
587 <https://doi.org/10.1029/2009jd011848>, 2009.

588 Herman, J., Evans, R., Cede, A., Abuhassan, N., Petropavlovskikh, I., and McConville, G.: Comparison
589 of ozone retrievals from the Pandora spectrometer system and Dobson spectrophotometer in Boulder,
590 Colorado, *Atmos. Meas. Tech.*, *8*, 3407–3418, <https://doi.org/10.5194/amt-8-3407-2015>, 2015.

591 Holmes, C. D., Bertram, T. H., Confer, K. L., Graham, K. A., Ronan, A. C., Wirks, C. K., and Shah, V.:
592 The Role of Clouds in the Tropospheric NO_x Cycle: A New Modeling Approach for Cloud Chemistry
593 and Its Global Implications, *Geophys. Res. Lett.*, *46*, 4980–4990, <https://doi.org/10.1029/2019GL081990>,
594 2019.

595 Hu, L., Keller, C. A., Long, M. S., Sherwen, T., Auer, B., Da Silva, A., Nielsen, J. E., Pawson, S.,
596 Thompson, M. A., Trayanov, A. L., Travis, K. R., Grange, S. K., Evans, M. J., and Jacob, D. J.: Global
597 simulation of tropospheric chemistry at 12.5 km resolution: Performance and evaluation of the GEOS-
598 Chem chemical module (v10-1) within the NASA GEOS Earth system model (GEOS-5 ESM), *Geosci.*
599 *Model Dev.*, *11*, 4603–4620, <https://doi.org/10.5194/gmd-11-4603-2018>, 2018.

600 Jacob, D. J., Heikes, B. G., Fan, S. M., Logan, J. A., Mauzerall, D. L., Bradshaw, J. D., Singh, H. B.,
601 Gregory, G. L., Talbot, R. W., Blake, D. R., and Sachse, G. W.: Origin of ozone and NO_x in the tropical
602 troposphere: A photochemical analysis of aircraft observations over the South Atlantic basin, *J. Geophys.*
603 *Res. Atmos.*, *101*, 24235–24250, <https://doi.org/10.1029/96jd00336>, 1996.

604 L Laughner, J., Zhu, Q., and Cohen, R. C.: Evaluation of version 3.0B of the BEHR OMI NO₂ product,
605 *Atmos. Meas. Tech.*, *12*, 128–146, <https://doi.org/10.5194/amt-12-129-2019>, 2019.

606 Lamsal, L. N., Martin, R. V., van Donkelaar, A., Steinbacher, M., Celarier, E. A., Bucsela, E., Dunlea, E.,
607 J., and Pinto, J. P.: Ground-level nitrogen dioxide concentrations inferred from the satellite-borne Ozone
608 Monitoring Instrument, *J. Geophys. Res. Atmos.*, *113*, 1–15, <https://doi.org/10.1029/2007JD009235>,
609 2008.

610 Lamsal, L. N., Martin, R. V., Padmanabhan, A., Van Donkelaar, A., Zhang, Q., Sioris, C. E., Chance, K.,
611 Kurosu, T. P., and Newchurch, M. J.: Application of satellite observations for timely updates to global
612 anthropogenic NO_x emission inventories, *Geophys. Res. Lett.*, *38*,
613 <https://doi.org/10.1029/2010GL046476>, 2011.

614 Laughner, J. and Cohen, R. C.: Direct observation of changing NO, *Science* (80-.), *366*, 723–727, 2019.

615 Laughner, J. L., Zhu, Q., and Cohen, R. C.: The Berkeley High Resolution Tropospheric NO₂ product,
616 *Earth Syst. Sci. Data*, *10*, 2069–2095, <https://doi.org/10.5194/essd-10-2069-2018>, 2018.

617 Li, C., Martin, R. V., Cohen, R. C., Bindle, L., Zhang, D., Chatterjee, D., Weng, H., and Lin, J.: Variable
618 effects of spatial resolution on modeling of nitrogen oxides, *Atmos. Chem. Phys.*, *23*, 3031–3049,
619 <https://doi.org/10.5194/acp-23-3031-2023>, 2023a.

620 Li, J., Wang, Y., Zhang, R., Smeltzer, C., Weinheimer, A., Herman, J., Boersma, K. F., Celarier, E. A.,
621 Long, R. W., Szykman, J. J., Delgado, R., Thompson, A. M., Knepp, T. N., Lamsal, L. N., Janz, S. J.,
622 Kowalewski, M. G., Liu, X., and Nowlan, C. R.: Comprehensive evaluations of diurnal NO₂
623 measurements during DISCOVER-AQ 2011: Effects of resolution-dependent representation of NO_x

624 emissions, *Atmos. Chem. Phys.*, 21, 11133–11160, <https://doi.org/10.5194/acp-21-11133-2021>, 2021.

625 Li, Y., Martin, R. V., Li, C., Boys, B. L., van Donkelaar, A., Meng, J., and Pierce, J. R.: Development and
626 evaluation of processes affecting simulation of diel fine particulate matter variation in the GEOS-Chem
627 model, *Atmos. Chem. Phys.*, 23, 12525–12543, <https://doi.org/10.5194/acp-23-12525-2023>, 2023b.

628 Lin, J. T. and McElroy, M. B.: Impacts of boundary layer mixing on pollutant vertical profiles in the
629 lower troposphere: Implications to satellite remote sensing, *Atmos. Environ.*, 44, 1726–1739,
630 <https://doi.org/10.1016/j.atmosenv.2010.02.009>, 2010.

631 GMDD - Improved Advection, Resolution, Performance, and Community Access in the New Generation
632 (Version 13) of the High Performance GEOS-Chem Global Atmospheric Chemistry Model (GCHP):
633 <https://gmd.copernicus.org/preprints/gmd-2022-42/>, last access: 18 June 2022.

634 Millet, D. B., Baasandorj, M., Farmer, D. K., Thornton, J. A., Baumann, K., Brophy, P., Chaliyakunnel,
635 S., De Gouw, J. A., Graus, M., Hu, L., Koss, A., Lee, B. H., Lopez-Hilfiker, F. D., Neuman, J. A., Paulot,
636 F., Peischl, J., Pollack, I. B., Ryerson, T. B., Warneke, C., Williams, B. J., and Xu, J.: A large and
637 ubiquitous source of atmospheric formic acid, *Atmos. Chem. Phys.*, 15, 6283–6304,
638 <https://doi.org/10.5194/acp-15-6283-2015>, 2015.

639 Murray, L. T., Jacob, D. J., Logan, J. A., Hudman, R. C., and Koshak, W. J.: Optimized regional and
640 interannual variability of lightning in a global chemical transport model constrained by LIS/OTD satellite
641 data, *J. Geophys. Res. Atmos.*, 117, 1–14, <https://doi.org/10.1029/2012JD017934>, 2012.

642 Nault, B. A., Garland, C., Pusede, S. E., Wooldridge, P. J., Ullmann, K., Hall, S. R., and Cohen, R. C.:
643 Measurements of CH₃O₂NO₂ in the upper troposphere, *Atmos. Meas. Tech.*, 8, 987–997,
644 <https://doi.org/10.5194/amt-8-987-2015>, 2015.

645 Oak, Y. J., Park, R. J., Schroeder, J. R., Crawford, J. H., Blake, D. R., Weinheimer, A. J., Woo, J. H.,
646 Kim, S. W., Yeo, H., Fried, A., Wisthaler, A., and Brune, W. H.: Evaluation of simulated O₃ production
647 efficiency during the KORUS-AQ campaign: Implications for anthropogenic NO_x emissions in Korea,
648 *Elementa*, 7, <https://doi.org/10.1525/elementa.394>, 2019.

649 Reed, A. J., Thompson, A. M., Kollonige, D. E., Martins, D. K., Tzortziou, M. A., Herman, J. R.,
650 Berkoff, T. A., Abuhassan, N. K., and Cede, A.: Effects of local meteorology and aerosols on ozone and
651 nitrogen dioxide retrievals from OMI and Pandora spectrometers in Maryland, USA during DISCOVER-
652 AQ 2011, *J. Atmos. Chem.*, 72, 455–482, <https://doi.org/10.1007/s10874-013-9254-9>, 2015.

653 Russell, A. R., Perring, A. E., Valin, L. C., Bucsela, E. J., Browne, E. C., Wooldridge, P. J., and Cohen,
654 R. C.: A high spatial resolution retrieval of NO₂ column densities from OMI: Method and evaluation,
655 *Atmos. Chem. Phys.*, 11, 8543–8554, <https://doi.org/10.5194/acp-11-8543-2011>, 2011.

656 Shah, V., Jacob, D. J., Li, K., Silvern, R., Zhai, S., Liu, M., Lin, J., and Zhang, Q.: Effect of changing
657 NO_x lifetime on the seasonality and long-term trends of satellite-observed tropospheric NO₂ columns
658 over China, *Atmos. Chem. Phys.*, 20, 1483–1495, <https://doi.org/10.5194/acp-20-1483-2020>, 2020.

659 Shah, V., Jacob, D. J., Dang, R., Lamsal, L. N., Strode, S. A., Steenrod, S. D., Boersma, K. F., Eastham,
660 S. D., Fritz, T. M., Thompson, C., Peischl, J., Bourgeois, I., Pollack, I. B., Nault, B. A., Cohen, R. C.,
661 Campuzano-Jost, P., Jimenez, J. L., Andersen, S. T., Carpenter, L. J., Sherwen, T., and Evans, M. J.:
662 Nitrogen oxides in the free troposphere: Implications for tropospheric oxidants and the interpretation of
663 satellite NO₂ measurements, *Atmos. Chem. Phys.*, 23, 1227–1257, [https://doi.org/10.5194/acp-23-1227-](https://doi.org/10.5194/acp-23-1227-2023)
664 2023, 2023.

665 Simone, N. W., Stettler, M. E. J., and Barrett, S. R. H.: Rapid estimation of global civil aviation emissions
666 with uncertainty quantification, *Transp. Res. Part D Transp. Environ.*, 25, 33–41,

667 <https://doi.org/10.1016/j.trd.2013.07.001>, 2013.

668 Van Stratum, B. J. H., Vilá-Guerau De Arellano, J., Ouwersloot, H. G., Van Den Dries, K., Van Laar, T.
669 W., Martinez, M., Lelieveld, J., Diesch, J. M., Drewnick, F., Fischer, H., Hosaynali Beygi, Z., Harder, H.,
670 Regelin, E., Sinha, V., Adame, J. A., Sörgel, M., Sander, R., Bozem, H., Song, W., Williams, J., and
671 Yassaa, N.: Case study of the diurnal variability of chemically active species with respect to boundary
672 layer dynamics during DOMINO, *Atmos. Chem. Phys.*, 12, 5329–5341, [https://doi.org/10.5194/acp-12-](https://doi.org/10.5194/acp-12-5329-2012)
673 5329-2012, 2012.

674 Tao, Y., Huang, W., Huang, X., Zhong, L., Lu, S. E., Li, Y., Dai, L., Zhang, Y., and Zhu, T.: Estimated
675 acute effects of ambient ozone and nitrogen dioxide on mortality in the Pearl River Delta of southern
676 China, *Environ. Health Perspect.*, 120, 393–398, <https://doi.org/10.1289/ehp.1103715>, 2012.

677 Thornton, J. A., Wooldridge, P. J., and Cohen, R. C.: Atmospheric NO₂: In Situ laser-induced
678 fluorescence detection at parts per trillion mixing ratios, *Anal. Chem.*, 72, 528–539,
679 <https://doi.org/10.1021/ac9908905>, 2000.

680 Tong, L., Zhang, H., Yu, J., He, M., Xu, N., Zhang, J., Qian, F., Feng, J., and Xiao, H.: Characteristics of
681 surface ozone and nitrogen oxides at urban, suburban and rural sites in Ningbo, China, *Atmos. Res.*, 187,
682 57–68, <https://doi.org/10.1016/j.atmosres.2016.12.006>, 2017.

683 Valin, L. C., Russell, A. R., Hudman, R. C., and Cohen, R. C.: Effects of model resolution on the
684 interpretation of satellite NO₂ observations, *Atmos. Chem. Phys.*, 11, 11647–11655,
685 <https://doi.org/10.5194/acp-11-11647-2011>, 2011.

686 Vandaele, A. C., Hermans, C., Fally, S., Carleer, M., Colin, R., Mérienne, M. F., Jenouvrier, A., and
687 Coquart, B.: High-resolution Fourier transform measurement of the NO₂ visible and near-infrared
688 absorption cross sections: Temperature and pressure effects, *J. Geophys. Res. Atmos.*, 107, ACH 3-1-
689 ACH 3-12, <https://doi.org/10.1029/2001JD000971>, 2002.

690 Veefkind, J. P., Aben, I., McMullan, K., Förster, H., de Vries, J., Otter, G., Claas, J., Eskes, H. J., de
691 Haan, J. F., Kleipool, Q., van Weele, M., Hasekamp, O., Hoogeveen, R., Landgraf, J., Snel, R., Tol, P.,
692 Ingmann, P., Voors, R., Kruizinga, B., Vink, R., Visser, H., and Levelt, P. F.: TROPOMI on the ESA
693 Sentinel-5 Precursor: A GMES mission for global observations of the atmospheric composition for
694 climate, air quality and ozone layer applications, *Remote Sens. Environ.*, 120, 70–83,
695 <https://doi.org/10.1016/j.rse.2011.09.027>, 2012.

696 Verhoelst, T., Compernelle, S., Pinardi, G., Lambert, J. C., Eskes, H. J., Eichmann, K. U., Fjæraa, A. M.,
697 Granville, J., Niemeijer, S., Cede, A., Tiefengraber, M., Hendrick, F., Pazmiño, A., Bais, A., Bazureau,
698 A., Folkert Boersma, K., Bogner, K., Dehn, A., Donner, S., Elohov, A., Gebetsberger, M., Goutail, F.,
699 Grutter De La Mora, M., Gruzdev, A., Gratsea, M., Hansen, G. H., Irie, H., Jepsen, N., Kanaya, Y.,
700 Karagkiozidis, D., Kivi, R., Kreher, K., Levelt, P. F., Liu, C., Müller, M., Navarro Comas, M., PETERS, A.
701 J. M., Pommereau, J. P., Portafaix, T., Prados-Roman, C., Puentedura, O., Querel, R., Remmers, J.,
702 Richter, A., Rimmer, J., Cárdenas, C. R., De Miguel, L. S., Sinyakov, V. P., Stremme, W., Strong, K.,
703 Van Roozendaal, M., Pepijn Veefkind, J., Wagner, T., Wittrock, F., Yela González, M., and Zehner, C.:
704 Ground-based validation of the Copernicus Sentinel-5P TROPOMI NO₂ measurements with the NDACC
705 ZSL-DOAS, MAX-DOAS and Pandonia global networks, *Atmos. Meas. Tech.*, 14, 481–510,
706 <https://doi.org/10.5194/amt-14-481-2021>, 2021.

707 Weng, H., Lin, J., Martin, R., Millet, D. B., Jaeglé, L., Ridley, D., Keller, C., Li, C., Du, M., and Meng,
708 J.: Global high-resolution emissions of soil NO_x, sea salt aerosols, and biogenic volatile organic
709 compounds, *Sci. Data*, 7, 1–15, <https://doi.org/10.1038/s41597-020-0488-5>, 2020.

710 Yang, L. H., Jacob, D. J., Dang, R., Oak, Y. J., Lin, H., Kim, J., Zhai, S., Colombi, N. K., Pendergrass, D.

711 C., Beaudry, E., Shah, V., Feng, X., Yantosca, R. M., Chong, H., Park, J., Lee, H., Lee, W.-J., Kim, S.,
712 Kim, E., Travis, K. R., Crawford, J. H., and Liao, H.: Interpreting GEMS geostationary satellite
713 observations of the diurnal variation of nitrogen dioxide (NO₂) over East Asia, *EGUsphere*, 1–25, 2023a.

714 Yang, L. H., Jacob, D. J., Colombi, N. K., Zhai, S., Bates, K. H., Shah, V., Beaudry, E., Yantosca, R. M.,
715 Lin, H., Brewer, J. F., Chong, H., Travis, K. R., Crawford, J. H., Lamsal, L. N., Koo, J. H., and Kim, J.:
716 Tropospheric NO₂ vertical profiles over South Korea and their relation to oxidant chemistry: implications
717 for geostationary satellite retrievals and the observation of NO₂ diurnal variation from space, *Atmos.*
718 *Chem. Phys.*, 23, 2465–2481, <https://doi.org/10.5194/acp-23-2465-2023>, 2023b.

719 Zhang, D., Martin, R. V., Bindle, L., Li, C., Eastham, S. D., van Donkelaar, A., and Gallardo, L.:
720 Advances in Simulating the Global Spatial Heterogeneity of Air Quality and Source Sector Contributions:
721 Insights into the Global South, *Environ. Sci. Technol.*, 57, 6955–6964,
722 <https://doi.org/10.1021/acs.est.2c07253>, 2023.

723 Zhang, Y., Wang, Y., Chen, G., Smeltzer, C., Crawford, J., Olson, J., Szykman, J., Weinheimer, A. J.,
724 Knapp, D. J., Montzka, D. D., Wisthaler, A., Mikoviny, T., Fried, A., and Diskin, G.: Journal of
725 Geophysical Research : Atmospheres of DISCOVER-AQ 2011 observations, 1–13,
726 <https://doi.org/10.1002/2015JD024203>. Received, 2016.

727 Zhao, X., Fioletov, V., Cede, A., Davies, J., and Strong, K.: Accuracy, precision, and temperature
728 dependence of Pandora total ozone measurements estimated from a comparison with the Brewer triad in
729 Toronto, *Atmos. Meas. Tech.*, 9, 5747–5761, <https://doi.org/10.5194/amt-9-5747-2016>, 2016.

730
731
732
733
734
735
736
737
738
739
740
741
742
743
744
745
746

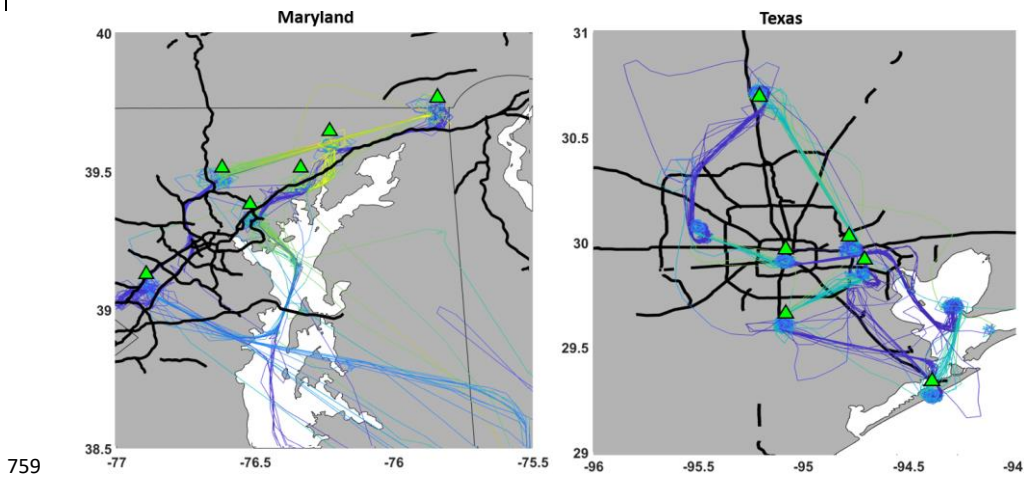
Formatted: Font: 12 pt, Bold

Formatted: Indent: Left: 0", First line: 0"

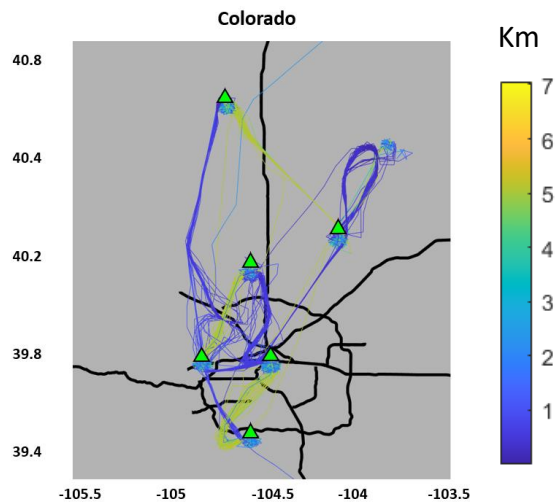
747
748
749
750
751
752
753
754
755
756
757
758

Appendix

Formatted: Indent: Left: 2.5"

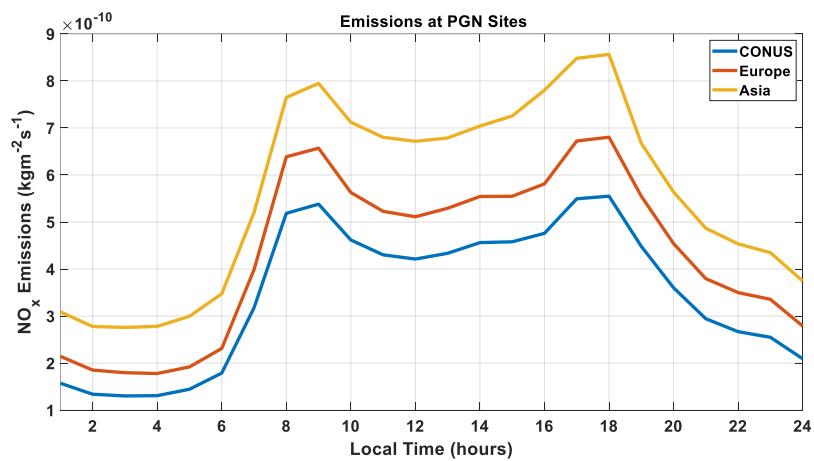


759



760
761

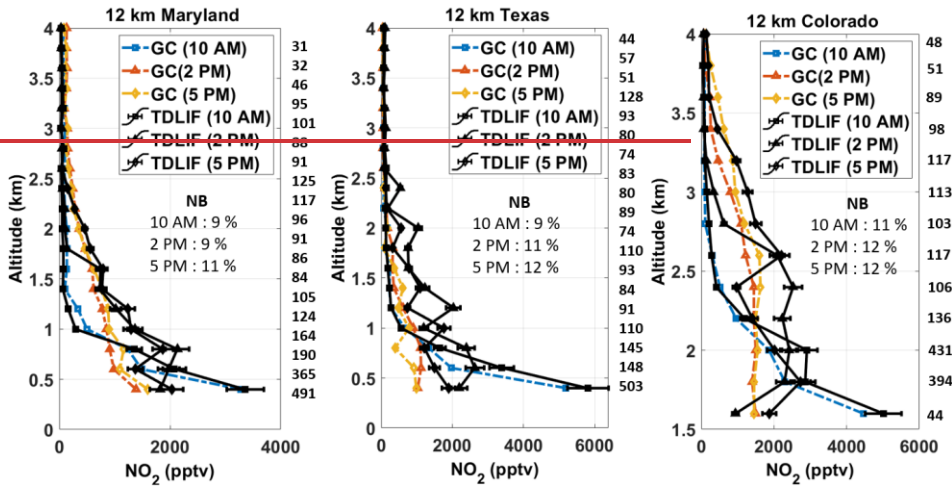
762 Figure A1. Flight tracks showing the path and altitude of the P-3B aircraft during the DISCOVER-AQ
763 campaign over Maryland during July 2011 (left), over Texas during September 2013 (center) and over
764 Colorado during July-August 2014 (right). The green triangles show the locations of the Pandora sun
765 photometers that have been used in this study. The Sites names and coordinates are listed in Table A1. Grey
766 indicates land, white indicates water. The black bold lines indicate roads.



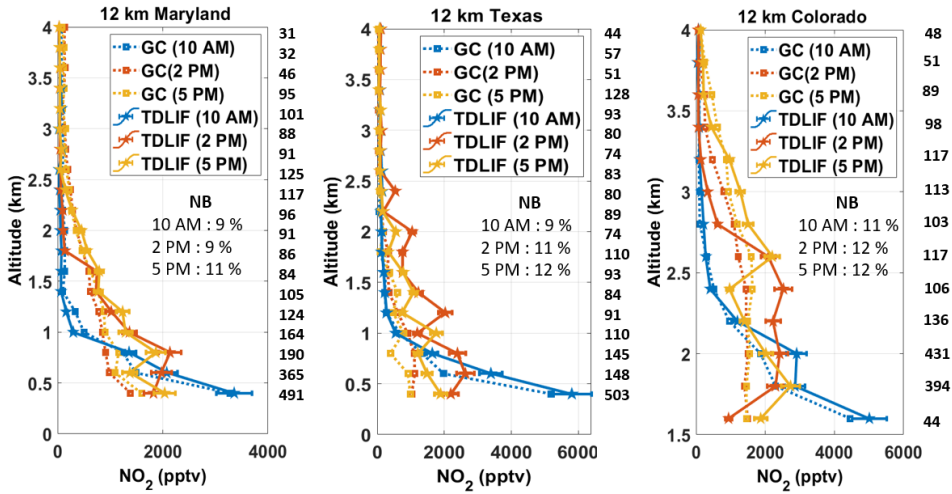
767

768 Figure A2. Hourly variation of NO_x emissions including all sectors across 50 PGN sites over the CONUS,
769 Europe, and east Asia.

770



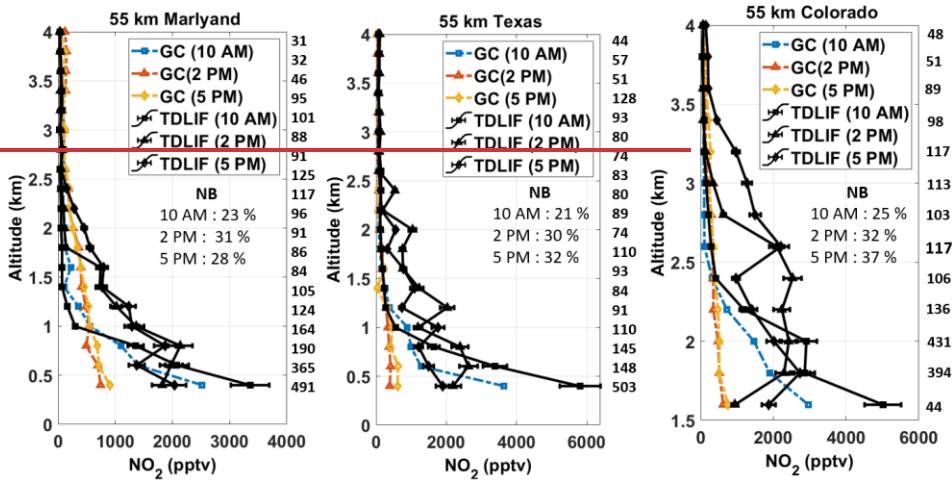
771



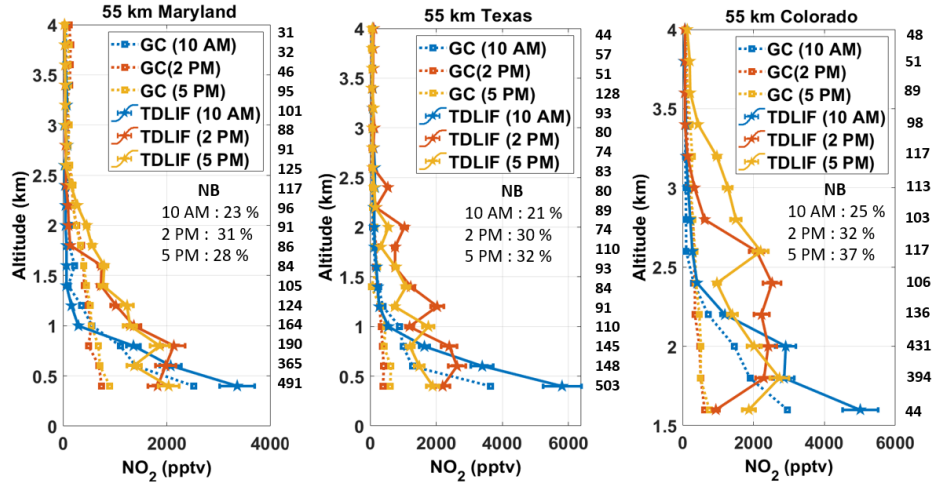
772

773 Figure A3: NO₂ Vertical profiles from TD-LIF instrument aboard during the DISCOVER-AQ campaign
 774 over Maryland, Texas and Colorado. ~~The black NO₂ vertical profiles from TD-LIF instrument aboard P-3B~~
 775 ~~during the DISCOVER-AQ campaign over Maryland, Texas and Colorado. The colored solid lines with~~
 776 ~~pentagram markers represent observations (square: 10 AM, triangle: 2 PM, diamond: 5 PM). The dotted~~
 777 ~~colored lines with square markers represent GCHP-12 km GCHP simulated NO₂-mixing ratios without~~
 778 ~~modifying the PBLH (blue: 10 AM, orange: 2 PM, yellow: 5 PM). The inset values in the boxes show the~~
 779 NB at 10 AM, 2 PM, and 5 PM. The numbers in the middle represent the number the observations associated
 780 with the corresponding altitude level. Error bars indicate standard errors in measurements.

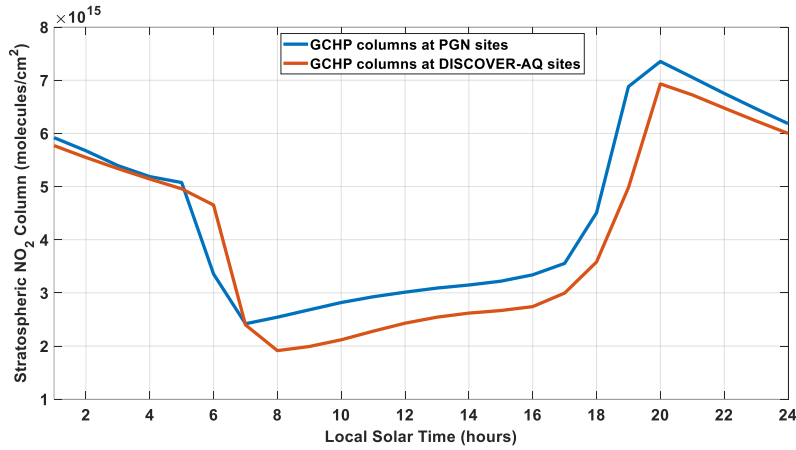
781



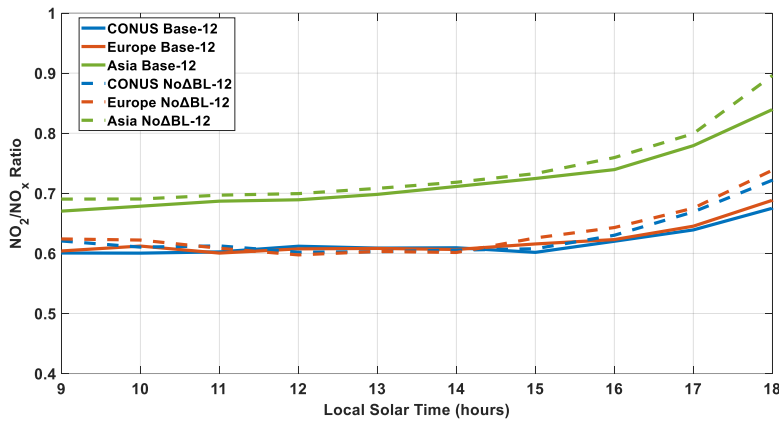
782



783 Figure A4: NO₂ Vertical profiles from TD-LIF instrument aboard during the DISCOVER-AQ campaign
 784 over Maryland, Texas and Colorado. ~~The black NO₂ vertical profiles from TD-LIF instrument aboard P-3B~~
 785 ~~during the DISCOVER-AQ campaign over Maryland, Texas and Colorado. The colored solid lines with~~
 786 ~~pentagram markers represent observations (square: 10 AM, triangle: 2 PM, diamond: 5 PM). The dotted~~
 787 ~~colored lines with square markers represent 12 km GCHP 55 km-simulated NO₂-mixing ratios without~~
 788 ~~modifying the PBLH (blue: 10 AM, orange: 2 PM, yellow: 5 PM). The inset values in the boxes show the~~
 789 NB at 10 AM, 2 PM, and 5 PM. The numbers in the middle represent the number the observations associated
 790 with the corresponding altitude level. Error bars indicate standard errors in measurements.

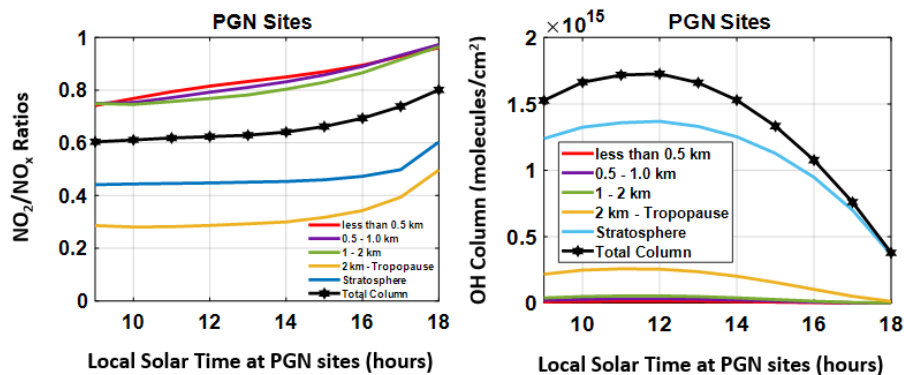


791
 792 Figure A5. GCHP NO₂ stratospheric columns for the three-month average of June-July-August at
 793 DISCOVER-AQ sites (red) and PGN sites (blue).



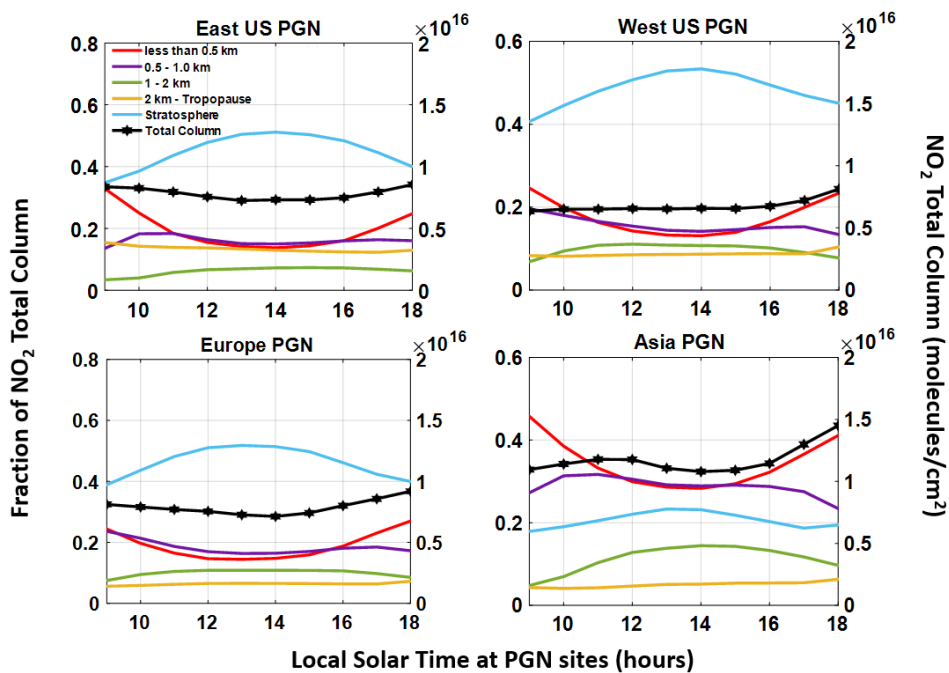
794
 795 Figure A6. Hourly variation of 12 km simulated column NO₂/NO_x ratios across 50 PGN sites over the
 796 CONUS (red), Europe (blue), and east Asia (green). The dotted lines show the 12 km simulated NO₂/NO_x
 797 ratios without modified PBLH.

798



799
 800 Figure A7. Simulated NO_2/NO_x ratios (left panel) and simulated partial and total OH columns (right panel)
 801 at different hours of the day averaged over the summer months of June-July-August for 2019 for PGN sites
 802 over the eastern US, western US, Europe, and eastern Asia.

Formatted: Font: 12 pt



804
 805 Figure A8. The simulated fractional contribution of NO_2 columns at different hours of the day averaged
 806 over the summer months of June-July-August for 2019 for PGN sites over the eastern US, western US,
 807 Europe, and eastern Asia. The right Y-axis shows the total columns of NO_2 .

808
 809 Table A1. Site name, latitude and longitude for 18 sites in Texas, Maryland, and Colorado that has
 810 concurrent pandora and aircraft measurements.

811

812

Site	Sites name	Latitude	Longitude	Date
813	Texas Sites			September 2013
814	1. Channelview	29.802	-95.125	
815	2. Conroe	30.350	-95.425	
816	3. Deer Park	29.670	-95.128	
817	4. Galveston	29.254	-95.861	
818	5. Manvel Croix	29.520	-95.392	
819	6. Moody Tower	29.718	-95.341	
820	Maryland Sites			July 2011
821	1. Aldino	39.563	-76.204	
822	2. Beltsville	39.055	-76.878	
823	3. Edgewood	39.410	-76.297	
824	4. Essex	39.311	-76.474	
825	5. Fairhill	39.701	-75.860	
826	6. Padonia	39.461	-76.631	
827	Colorado Sites			July-August 2014
828	1. Bao Tower	40.043	-105.012	
829	2. Chatfield Park	39.535	-105.074	
830	3. Denver La Casa	39.782	-105.018	
831	4. Fort Collins	40.595	-105.143	
832	5. Platteville	40.183	-104.734	
833	6. NREL-Golden	39.743	-105.181	

834
 835 Table A2. Site name, latitude and longitude for 31 sites in CONUS and 11 sites in Europe, North
 836 Africa and Middle-east, and 9 sites in east Asia from the PGN database.

Site	Site Name	Latitude	Longitude	Date
Eastern US			June-July-August 2019	
1.	'Bristol_PA'	40.1074	-74.8824	
2.	'Cambridge_MA'	42.3800	-71.1100	
3.	'CapeElizabeth_ME'	43.5610	-70.2073	
4.	'ChapelHill_NC'	35.9708	-79.0933	
5.	'CharlesCity_VA'	37.3260	-77.2057	
6.	'Dearborn_MI'	42.3067	-83.1488	
7.	'Detroit_MI.txt'	42.3026	-83.1068	
8.	'Hampton_VA'	37.0203	-76.3366	
9.	'Londonderry_NH'	42.8625	-71.3801	
10.	'Lynn_MA'	42.4746	-70.9708	
11.	'Madison_CT'	41.2568	-72.5533	
12.	'Manhattan_NY'	40.8153	-73.9505	
13.	'NewBrunswick_NJ'	40.4622	-74.4294	
14.	'NewHaven_CT'	41.3014	-72.9029	
15.	'OldField_NY'	40.9635	-73.1402	
16.	'Philadelphia_PA'	39.9919	-75.0811	
17.	'Pittsburgh_PA '	40.4655	-79.9608	
18.	'WallopsIsland_VA '	37.8439	-75.4775	
19.	'WashingtonDC'	38.9218	-77.0124	
20.	'Westport_CT'	41.1183	-73.3367	

Western US

June-July-August 2019

21.	'Aldine_TX'	29.9011	-95.3262
22.	'Boulder_CO'	40.0375	-105.2420
23.	'Edwards_CA '	34.9600	-117.8811
24.	'Houston_TX'	29.7200	-95.3400
25.	'LaPorte_TX'	29.6721	-95.0647
26.	'Manhattan_KS'	39.1022	-96.6096
27.	'MountainView_CA'	37.4200	-122.05680
28.	'Richmond_CA'	37.9130	-122.3360
29.	'SaltLakeCity_UT'	40.7663	-111.8478
30.	'SouthJordan_UT'	40.5480	-112.0700
31.	'Wrightwood_CA'	34.3819	-117.6813

Europe

June-July-August 2019

32.	'Athens'	37.9878	23.7750
33.	'Bremen'	53.0813	8.8126
34.	'Brussels'	50.7980	4.3580
35.	'Cologne'	50.9389	6.9787
36.	'Davos'	46.8000	9.8300
37.	'Innsbruck'	47.2643	11.3852
38.	'Juelich'	50.9080	6.4130
39.	'Lindenberg'	52.2900	14.1200
40.	'Rome'	42.1057	12.6402
41.	'Tel-Aviv'	32.1129	34.8062

Eastern Asia

June-July-August 2019

42.	'Beijing'	40.0048	116.3786
43.	'Kobe'	34.7190	135.2900
44.	'Sapporo'	43.0727	141.3459
45.	'Seosan'	36.7769	126.4938
46.	'Seoul'	37.5644	126.9340
47.	'Tokyo'	35.6200	139.3834
48.	'Tsukuba'	36.0661	140.1244
49.	'Ulsan'	35.5745	129.1896
50.	'Yokosuka'	35.3207	139.6508

838

839 Table A3. Sectoral contribution to NOx emissions averaged over all PGN sites, the US, Europe
840 and Asia.

PGN Sites	TRA(%)	RCO(%)	IND(%)	ENE(%)	SHP(%)	AGR(%)	WST(%)
ALL	49	19	13	7	7	4	1
CONUS	45	29	16	4	2	3	1
Europe	47	11	8	10	16	7	1
Asia	55	12	15	9	4	3	2

841

842 TRA: Transport, RCO: Residential Combustion, IND: Industry, ENE: Energy, SHP: Ship Emissions, AGR:
843 Agriculture, WST: Waste

844